ELECTRICAL CONDUCTION MECHANISMS IN THE DISORDERED MATERIAL SYSTEM p-TYPE HYDROGENATED AMORPHOUS SILICON

Kiran Shrestha, B.Sc., M.Sc., M.S.

Dissertations Prepared for the Degree of

DOCTOR OF PHILOSOPHY

UNIVERSITY OF NORTH TEXAS

December 2014

APPROVED:

Chris L. Littler, Co-major Professor and Chair of the Department of Physics
A.J. Syllaios, Co-major Professor
Usha Philipose, Committee Member
Duncan Weathers, Committee Member
Mark Wardell, Dean of the Toulouse Graduate School

Shrestha, Kiran. Electrical Conduction Mechanisms in the Disordered Material System P-Type Hydrogenated Amorphous Silicon. Doctor of Philosophy (Physics), December 2014, 81 pp, 6 tables, 35 illustration, references, 74 numbered titles.

The electrical and optical properties of boron doped hydrogenated amorphous silicon thin films (a-Si) were investigated to determine the effect of boron and hydrogen incorporation on carrier transport. The a-Si thin films were grown by plasma enhanced chemical vapor deposition (PECVD) at various boron concentrations, hydrogen dilutions, and at differing growth temperatures. The temperature dependent conductivity generally follows the hopping conduction model. Above a critical temperature, the dominant conduction mechanism is Mott variable range hopping conductivity (M-VRH), where $p = 1/4$, and the carrier hopping depends on energy. However, at lower temperatures, the coulomb interaction between charge carriers becomes important and Efros-Shklosvkii variable hopping (ES-VRH) conduction, where $p=1/2$, must be included to describe the total conductivity. To correlate changes in electrical conductivity to changes in the local crystalline order, the transverse optical (TO) and transverse acoustic (TA) modes of the Raman spectra were studied to relate changes in short- and mid-range order to the effects of growth temperature, boron, and hydrogen incorporation. With an increase of hydrogen and/or growth temperature, both short and mid-range order improve, whereas the addition of boron results in the degradation of short range order. It is seen that there is a direct correlation between the electrical conductivity and changes in the short and mid-range order resulting from the passivation of defects by hydrogen and the creation of trap states by boron. This work was done under the ARO grant W911NF-10-1-0410, William W. Clark Program Manager. The samples were provided by L-3 Communications.

Copyright 2014

By

Kiran Shrestha

ACKNOWLEDGEMENTS

I am very grateful to many people in the journey of my graduate studies and my PhD work. First and foremost, I am very fortunate and honored to have Prof. Chris. L. Littler and Prof. A. J. Syllaios as my co-major advisors. I will be forever grateful and thankful to both my advisors, who have taken me as a graduate student and trained me to work in the research field to setup from scratch. I am deeply indebted to Prof. Syllaios and Prof. Littler for their continuous support both financially and academically by providing valuable advice.

I would like to thank Prof. Vince Lopes, who taught me a lot to become an experimental physicist. Many thank go to Prof. Duncan Weathers and Prof. Usha Philipose for serving as committee member and providing valuable suggestions and encouragement. I would like to thank my collaborators, all friends of UNT and colleagues who worked with me and helped me. Support from the engineers of the UNT Physics electronics lab and machine shop was remarkable. I would like to thank the Department of Physics at UNT, including all faculty members, for giving me the opportunity to study here.

I would like to acknowledge generous financial support from the Army Research Office and special thanks to Dr. William Clark, Program Manager of ARO. I acknowledge L-3 communications for providing samples for this study as necessary to carry out my research.

Finally, I cannot find the words to express my thanks and gratitude for my wife, Binita Mool, and our parents for all the dreams they sacrificed to make my dream come true. I would have never succeeded without support of my entire family members. Finally, I do not know how to thank my son Jeebesh and daughter Jeshina during my graduate student life in the USA.

Dedicated to my parents, brother, sisters and entire family

TABLE OF CONTENTS

Page

ACKNOWLEDGEMENTS iii

LIST OF TABLES vi

LIST OF ILLUSTRATIONS vii

CHAPTER 1 INTRODUCTION 1

1.1 Background 1

1.2 Phase Diagram of a-Si:H Thin Film Growth Evolution 4

1.3 Density of States (DOS) 6

1.4 Bonding Of Hydrogen With Silicon Atoms in a-SI:H 7

1.5 Boron in a-Si: H 10

1.6 Highlights Of The Results of The Dissertation 11

CHAPTER 2 ELECTRICAL CHARACTERIZATION OF a-Si:H THIN FILMS 12

2.1 General Introduction and Theory of Electrical Conduction in Amorphous Semiconductors 12

2.2 Temperature Coefficient of Resistance (TCR) 18

2.3 Sample Information 19

2.4 Electrical Conductivity and TCR Measurements 21

2.5 Results and Discussion 23

2.6 Summary and Conclusion 53

CHAPTER 3 OPTICAL CHARACTERIZATION 55

3.1 Raman Spectroscopy 55

3.2 Experimental 58

3.3 Results and Discussion 58

3.4 Summary and Conclusion 68

CHAPTER 4 SUMMARY/ CONCLUSION/ FUTURE DIRECTIONS 69

APPENDIX X-RAY PHOTOELECTRON SPECTRA (XPS) of REPRESENTATIVE AMORPHOUS SILICON THIN FILM 72

REFERENCES 74

LIST OF TABLES

Page

Table 1. Parameters determined by Mott-fitting of conductivity and TCR data.......................... 33

Table 2. Conductivity prefactors and characteristic temperatures... 36

Table 3. Sample properties - various parameters described in the text. 47

Table 4. Calculations of wave function localization length 49

Table 5. Calculations of wave function localization length 51

Table 6. Raman parameters.. 66

LIST OF ILLUSTRATIONS

Page

Figure 1-1. The phase diagram showing growth evolution of a-Si:H thin films 5

Figure 1-2. Density of state for the p-type a-Si:H, showing the mobility gap energy[1] 7

Figure 1-3. Structural configuration of hydrogen in a-Si:H[30] 8

Figure 2-1. Hopping between the two localized states 13

Figure 2-2. Sample structure showing different insulating layers 20

Figure 2-3. Schematic of device structure fabricated at L-3 Communications 20

Figure 2-4. Block diagram of equipment used to measure Van der Pauw resistivity 22

Figure 2-5. Resistivity and Hall Effect measurement Equipment (photograph).......................... 23

Figure 2-6. Temperature dependent conductivity of various samples 24

Figure 2-7. Room temperature conductivity vs. R_H for fixed boron doping 25

Figure 2-8. Conductivity of a-Si:H thin film (~1000 Å thick) 26

Figure 2-9. Conductivity of a-Si:H thin film (~500 Å thick) 27

Figure 2-10. Log conductivity vs. $T^{-1/4}$ and Log conductivity vs. $T^{-1/2}$ 29

Figure 2-11. Illustration of the RCDA method 31

Figure 2-12. RCDA of a-Si:H samples for fixed R_H and various doping levels 32

Figure 2-13. TCR of the samples with fixed R_H and three different “r” values 33

Figure 2-14. Conductivity vs. $T^{-1/4}$ 34

Figure 2-15. Temperature dependent conductivity for R_H=4 35

Figure 2-16. Temperature dependent conductivity for R_H 16 36

Figure 2-17. Conductivity and TCR vs. Temperature 37

Figure 2-18. TCR data and the TCR fit for samples having fixed r and varying R_H 38

Figure 2-19. TCR_Mott vs. R_H at fixed “r”=0.32 and TCR_Mott vs. “r” at fixed R_H=60 41

Figure 2-20. TCR_Mott vs. resistivity for fixed boron doping 42

Figure 2-21. TCR_Mott vs. RT resistivity of various samples having different R_H and “r” 43

Figure 2-22. Ln σ_{0M} plotted against T_{0M}. 44

Figure 2-23. Resistivity vs. T_{0M} at RT 46

Figure 2-24. T_{0M} vs. R_H 48

Figure 2-25. T_{oM} and localization length vs. R_H for the samples having fixed doping ratio “r”=0.32 50

Figure 2-26. T_{oM} and localization length vs. boron doping for fixed R_H=60 51

Figure 3-1. (a) Raman Spectrometer (UNT-CART) (b) Raman sample structure 56

Figure 3-2. Representative Raman spectra for the doping level 61

Figure 3-3. Γ_{TO} vs. H-dilution 63

Figure 3-4. (a) Γ_{TO} vs. boron incorporation, “r”, and (b) Γ_{TO} vs. H-dilution, R_H. 65

Figure 3-5. Line width and central frequency of TO mode vs. RT resistivity 67

CHAPTER 1

INTRODUCTION

1.1 Background

The semiconductor hydrogenated amorphous silicon (a-Si:H) is found in many technological applications, such as solar cells, thin film transistors, and focal plane arrays[1]. One of these is as an infrared detector, where the sensing of infrared radiation is accomplished through bolometric means. Cameras based on a-Si:H detectors are marketed by a number of companies such as L-3 Communications[2], Sofradir[3] and ULIS[4]. Detectors manufactured using a-Si:H are preferred due to ease of manufacture and compatibility with silicon manufacturing processes, leading to low cost. In this type of infrared detector, the thermal energy is captured, warming the sensor and producing a change in the resistivity of the material. Therefore, a better understanding of electrical conduction mechanisms in a-Si:H is important for improvement in the performance of these devices.

Over the past two decades, both undoped and doped a-Si:H have exhibited interesting temperature dependent conductivity. This conductivity was first described by Mott[5], where the electrical conduction was shown to take place via the hopping of charge carriers from electrically-active defect states (traps) to other traps with binding energies in the vicinity of Fermi level. In the Mott model, the density of states (DOS) is assumed to be constant. This Mott variable range hopping (M-VRH) model has been extensively used to explain electrical conduction in a-Si:H[6,7,8]. In addition, researchers studying different disordered material systems have also adopted the M-VRH model to describe the temperature-dependent conductivity in their materials.

As measurements of disordered materials improved, other carrier hopping mechanisms, such as the Efros Skhlovskii-variable range hopping (ES-VRH), nearest neighbor hopping (NNH), and thermal activation processes have been used to describe the temperature dependence of the conductivity in various disordered semiconductors[9,10,11] in temperature regimes where M-VRH did not provide an adequate description. For example, Narjis et al[12] observed a transition between ES-VRH and M-VRH in a hydrogenated amorphous silicon-nickel alloy at low temperatures. Similarly, various different materials, Sn O_2[13], InGaN[14], PbSe[11], a-SiGe[15] show variable range hopping mechanisms with cross-over between Mott and ES, or NNH and ES. In addition, Yildiz et al[16] reported a cross-over from NNH to ES-VRH in n-type a-Si:H. For p-type a-Si:H, Crupi et al[17] reported only seeing thermal activation in PECVD (plasma enhanced chemical vapor deposition) grown, boron doped a-Si:H in a temperature range 275K to 400K, indicating the conduction occurs only through extended states. For a-Si thin films, Savvides[18] reported on a comprehensive study of the effects of boron doping and H-dilution. In his work, the samples were prepared by magnetron reactive sputtering, with boron doping accomplished using B_2H_6. The thickness of the film ranged between 5000-10000 Å, and the growth temperature was 225° C. For the boron doped samples, it was observed that the M-VRH alone described the temperature dependence of the conductivity. Other undoped samples with hydrogen content between 0 to 30 at. % exhibited thermal activation at temperatures above 400K. However, at lower temperatures, M-VRH was not sufficient to describe the electrical conduction. Thus, the nature of electrical conduction in a-Si and similar disordered materials is complex and in need of further investigation.

Raman spectroscopy is another tool that can be used to understand disordered materials such as a-Si:H.[19,20] It has been well established that an increase in the line-width of transverse optical (TO) mode is associated with an increase in the silicon bond angle deviation, which is associated with a decrease in the Short Range Order (SRO) of the a-Si network. The integrated intensity of the transverse acoustic (TA) mode is used as a measure of mid-range order (MRO), as it is related to the density of fluctuations in the dihedral angle between the adjacent silicon tetrahedrons[21,22,23]. Z. Li et al[24] indicated that there is improvement in structure with an increase of Ar dilution with SiH_4 in the n-type amorphous hydrogenated silicon thin film.

Recently, A.J. Syllaios et al[25] observed in the Raman spectra of a-Si:H that an increase in Boron doping broadens the TO mode, indicating a retardation in the formation of microcrystals in the film, resulting in an increase in structural disorder. Due to the dopant gas, new bonding states appear in the thin film that increase the number of energy states in the thin film matrix.

In this work, extensive resistivity measurements obtained from samples of varying thickness, Boron doping, and H-dilution show that the electrical conductivity in a-Si is dominated by M-VRH. This assignment is further supported by a resistance curve derivative analysis (RCDA) of the electrical conductivity, confirming the temperature dependence predicted by the Mott conduction mechanism. However, for highly doped, lower dilution samples at lower temperatures, the conductivity deviates from that predicted by M-VRH and can be explained by a superposition of the M-VRH and ES-VRH conductivity mechanisms.

Raman spectroscopy measurements have been carried out on a representative set of a-Si:H samples to obtain information on the structural properties of the thin films which affect the electrical conduction. Raman results show that the SRO in a-Si improves with the increase of H-

dilution (R_H), and degrades with addition of boron. Samples grown at the higher substrate temperature show better SRO compared to the samples grown at the lower substrate temperature. The information obtained concerning SRO and MRO has provided new insight on the natures of the trap states that control the electrical conductivity. It has been observed by multiple internal reflections (MIR) infrared spectroscopy[26], that it is the boron residing in the a-Si matrix in non-substitutional sites, which contribute to trap states rather than substitutional acceptor impurities, increasing the trap states that contribute to electrical conduction.

This work both builds on and expands that of past studies, extending the range of a-Si samples investigated to include a much larger range of boron concentrations, H-dilutions, thicknesses, and substrate growth temperatures to provide a more detailed understanding of the role of doping and H-dilution in the trap states in a-Si:H.

Chapter Two details the electrical properties of a-Si:H. Temperature dependent electrical conductivity measurement will be presented and discussed in detail. In chapter three, the results of Raman spectroscopy measurements will be presented and discussed including correlations between Raman results and conductivity. Finally, in chapter four, the conclusions and a discussion of the future direction of this research will be presented.

1.2 Phase Diagram of a-Si:H Thin Film Growth Evolution

The material properties, including the electrical and optical characteristics of a-Si:H thin films depend strongly on growth parameters like temperature, growth conditions, and the addition of impurities. For PECVD prepared films, the following diagram shows the evolution of a-Si:H thin film growth.

As shown in Figure 1-1, an increase in H-dilution (R_H) results in a transition from amorphous to microcrystalline material, and the deposition rate decreases[27]. The amorphous to microcrystalline phase boundary depends both on the dilution ratio $R_H = [H_2]/[SiH_4]$ and the thickness of the film. As the thickness increases, ordered regions grow.

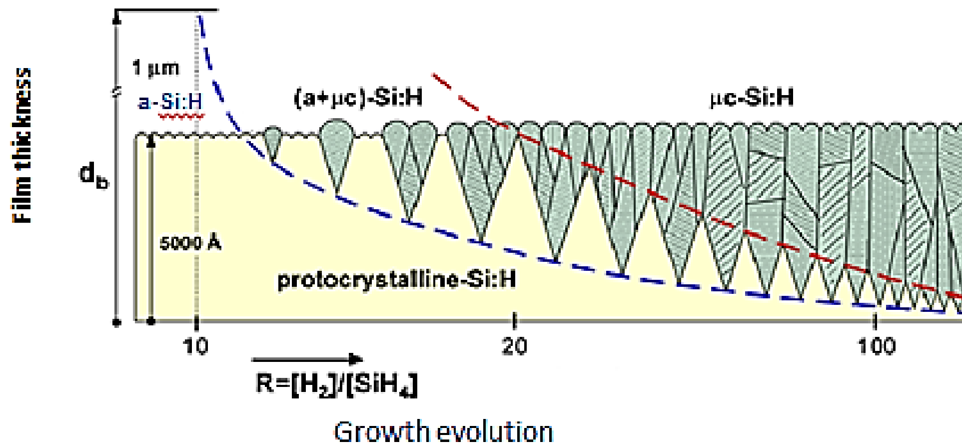

Figure 1-1. The phase diagram showing growth evolution of a-Si:H thin films[28]

As shown in Figure 1-1, the transition from amorphous to amorphous and microcrystalline (a+µC) is indicated by the dashed blue line and the transition from (a+µC) to microcrystalline (µC) transition by the dashed red line. Thus, a variety of phases can be present in a-Si:H thin films and the presence of each will modify the electrical conduction properties. For the investigations here, care is taken to grow thin films near the amorphous to (a+µC) transition, where the samples are almost completely amorphous.

In amorphous materials, trap states are present due to defects, dangling bonds, voids and microvoids, and impurities. A trap is a localized imperfection that is capable of capturing charge carriers. Traps affect the freedom of motion of the carriers.[29] At low temperatures in disordered materials, conduction occurs by the migration of charge carriers from one trap state to another in the vicinity of the Fermi level. If a variety of trap states exist, the distance from

one trap to another varies throughout the material, and the mechanism responsible for carrier transport is called “variable range hopping (VRH)”.

The states near the Fermi energy level, E_F, originate from defects and impurities, and hence the conductivity varies with the trap density. The effective band gap in a-Si:H is influenced by dangling bonds, bond energy distributions, voids, and strained bonds, all of which will influence the electrical properties. Hydrogen passivates the dangling bonds, reducing the total trap density that, in turn, affects the conductivity. In the next section the density of states for a-Si is discussed, including the influence of dopant and defect states.

1.3 Density of States (DOS)

In the case of amorphous silicon, there is no finite band edge as there is no well-defined periodicity of the potential energy. This results in the formation of “so called” band tails. As a result, amorphous silicon exhibits a quasi-continuous density of states that extends into the band gap, resulting in no well-defined valence or conduction band edge. Instead, there exists a “mobility edge”, which separates the extended states and the localized states. The difference between the energies of mobility edges in the valence and conduction bands is called mobility gap[1] and its value is close to 1.85 eV (Figure 1-2). Thus, the DOS is characterized by three regions: (i) extended states above the mobility edge of the conduction band, (ii) extended states below the mobility edge of the valence band, and (iii) localized states between the mobility edges, as shown in Figure 1-2.

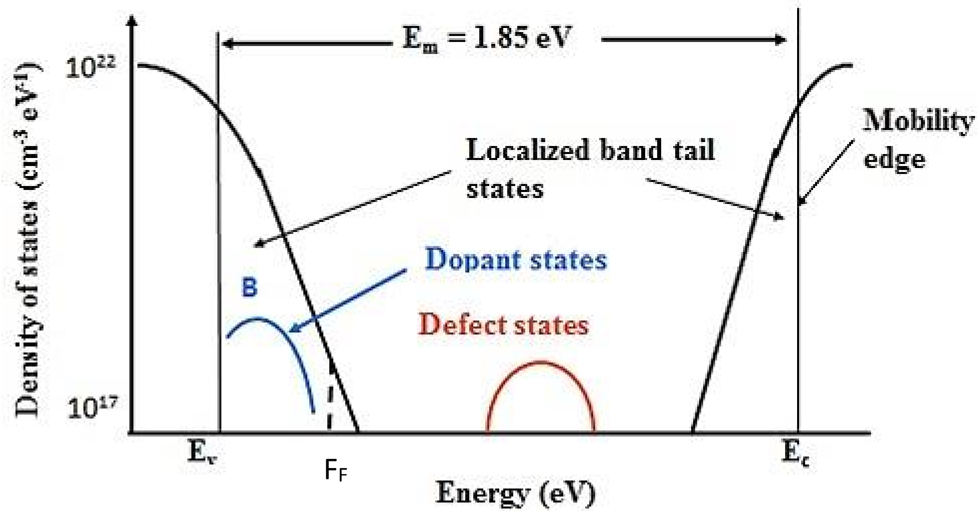

Figure 1-2. Density of state for the p-type a-Si:H, showing the mobility gap energy[1]

The dopant states reside in the valence band tail, as shown in Figure 1-2, and the Fermi level (E_F) is shown by the dotted vertical line. The dopant and the defect states influence the transport properties since they influence the carrier concentration at thermal equilibrium and determine the position of the Fermi level. These defect states also act as traps and recombination centers. Such traps influence the motion of charge carriers and thus the electrical properties.

1.4 Bonding Of Hydrogen With Silicon Atoms in a-SI:H

The addition of hydrogen in a-Si changes the electrical properties due to modifications of mobility gap as there is passivation of dangling bonds. There will also be a decrease in the dangling bonds as other bonds are formed (e.g., B-H, and Si-H_2, (Si-H_2)$_n$) in the amorphous silicon matrix. The quantity determining the incorporation of hydrogen in the a-Si matrix is the average binding energy of the hydrogen atom with respect to the lowest energy transport path in the amorphous network. This transport path is the motion of a single hydrogen atom via a

so-called 'bond center' (BC) site, where the hydrogen atom inserts itself symmetrically between its two nearest neighbor silicon atoms[30].

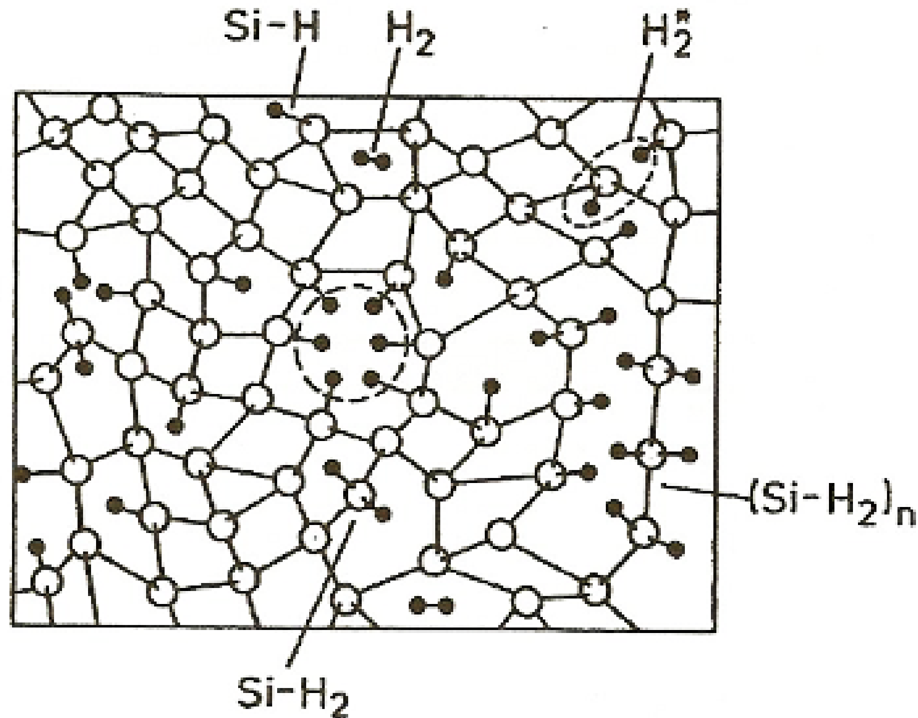

Figure 1-3. Structural configuration of hydrogen in a-Si:H[30]

Figure 1-3 illustrates how the monohydride (Si-H) and dihydride ($Si-H_2$) are arranged. In addition, there is a chain-like structure of polysilane ($Si-H_2$)n, the interstitial molecules H_2 and H_2*, and hydrogenated voids. These voids and microvoids are dependent on the method of growth and the deposition conditions, and can be measured by the SIMS[30] and the ellipsometry techniques[31]. The hydrogen is randomly dispersed with concentration of 2-3 at %, and the void surfaces comprise either Si-H or $Si-H_2$ bonds[33].The effects of voids and microvoids are manifested through the hydrogen bonding details that were studied by MIR-IR[26]. Hydrogen will reduce the dangling bonds by forming the Si-H bonds and break the weak bonds to Si-Si if there are not enough dangling bonds in the film to absorb the extra hydrogen. As a result, hydrogen

is capable of modifying the silicon bonding network during the deposition process. The introduction of hydrogen changes the structural, and hence optical and electrical properties of a-Si because hydrogen reduces the trap defect density via the reduction of dangling bonds. The formation of the Si-H bond causes an increase in the energy gap because the Si-H binding energy is greater than that of the Si-Si bond[32]. Different varieties of bond configurations (as seen in Figure 1-3) can exist in the silicon matrix, resulting in a wide range of binding energies (1 to 3.4 eV). The structural disorder of amorphous silicon introduces a large density of traps for isolated hydrogen. These traps capture hydrogen and form Si-H bonds. In Figure 1-3, the silicon forms a rigid non-equilibrium structure, whereas hydrogen has a mobile equilibrium structure. Hydrogen can be incorporated into the Si, and the stable bond Si-H is formed either by attaching to a dangling bond or through the breaking the weak Si-Si bond[33]. Further, two phases of hydrogen in a-Si:H are dilute and clustered, as evidenced in proton magnetic resonance[34] (Xunming et al, 2003) so that in a dilute phase a particular hydrogen atom is about 1nm away from any other hydrogen atom, and in the clustered phase there are two or more hydrogen atoms in close proximity. The H-dilution involves several effects, such as (i) atomic hydrogen etches a growing film there by removing strained weaker bonds, which located in energetically unfavorable locations, (ii) surface diffusivity of adatoms and the hydrogen atoms can move around to more energetically stable position and form stronger bonds, and (iii) atomic hydrogen diffuses into the network and improves the structure[34]. It is indicated by the *ab initio* method that the mobile hydrogen atom breaks strained silicon bonds to form Si-H and $Si\text{-}H_2$[35].

1.5 Boron in a-Si: H

In 1975, Spear and LeComber used diborane [B_2H_6][36] to introduce boron into a-Si:H by the method of glow discharge. The acceptor, boron, enters substitutionally into the a-Si matrix, occupying sites of tetrahedral coordination. Although the boron atom of B_2H_6 has a four-fold coordination, the bonding is distorted from a tetrahedral configuration[37] in a-Si:H. When incorporated into the a-Si matrix, there is formation of three coordinated groupings, such as BSi_3 and Si_2BH. Infrared studies by Chen and Cardona[38] and Tsai[37] indicated that there are three main vibrational stretching modes: Si-B (1400 cm^{-1}), B-H (2475cm^{-1}), and Si-H or Si-H_2 around 2000-2100 cm^{-1}. The B-H intensity is seen to increase with the addition of boron, whereas the Si-H and Si-H_2 vibrational modes intensity decrease. Therefore, a competition between boron and silicon to capture a hydrogen atom[26] exists. By comparing the silicon and boron peaks of Auger spectra[37], it is shown that the incorporation of boron as compared to silicon is independent of the growth temperature.

Referring to the Figure 1-2 the localized mid gap states are commonly associated with dangling bonds and band tail states in the valance and conduction bands. The tail states act as trapping centers. The dangling bonds are the defect states and Gaussian distribution were used to model the dangling bond states distribution[27]. A dangling bond can be neutral (D^0), positive (D^+) and negative (D^-). The dangling bonds can acts as acceptor for p-type material. These states could also contribute to the non-active boron doping configurations[39]. This doping results from the presence of intrinsic hole traps, which are associated with highly distorted bond angles in the a-Si:H matrix[39]. The densities of dopant and defect states are controlled by the position of the Fermi level[40], for boron doped material the E_F lies in the valance band tail and with the

increase of disorder due to boron, the width of band tails are broader. Defect states in the mid gap also get broader with the increase of disorders in the material. Wave functions of the defect and tail states are localized within the structure.

By first principle calculations, it has been proposed that a boron with three silicon and one hydrogen neighbors ((B (3, 1)) is the most energetically favorable doping configuration[41].

1.6 Highlights Of The Results of The Dissertation

The electrical transport properties were analyzed in various samples prepared by PECVD, which differ in H-dilution and boron doping. The study shows that in the hydrogenated amorphous silicon materials the electrical conductivity mechanism is best described by the Mott VRH mechanism; however, at low temperatures there is evidence of Efros-Shklovskii conduction. The TCR is also described by M-VRH in high temperature regime and at low temperatures by the combination of TCR_ES and TCR_Mott.

The structural properties obtained by Raman spectroscopic technique indicate that the SRO improves for higher H-dilution and degrades with the addition of boron. In addition, the growth temperature plays an important role in the structural properties, indicating that higher growth temperature shows better both SRO and MRO. The incorporation of boron degrades the SRO due to the formation of different B complexes. The IR technique[26] also shows that there is inverse relationship between H-dilution and boron doping, in agreement with the Raman results. A competition between boron and silicon to capture a hydrogen atom is seen and assists in the understanding of the correlation between SRO by Raman results with electrical resistivity. This may ultimately provide a new method for determining electrical conduction properties from purely optical measurements.

CHAPTER 2

ELECTRICAL CHARACTERIZATION OF a-Si:H THIN FILMS

2.1 General Introduction and Theory of Electrical Conduction in Amorphous Semiconductors

This chapter will focus on the theory of the electrical properties in a-Si:H, which includes models from the temperature dependence of the conductivity, and temperature coefficient of resistance (TCR). Following this discussion, the experimental methodology and results from transport measurements will be presented and discussed.

In a-Si:H, electric transport can take place through extended states in the conduction band, valence band and states in the mobility gap. Near the Fermi energy, if the states are localized, the probability "P" that carriers 'jump' from one localized state to another localized state of higher energy depends on three factors[5] .These are (a) the attempt frequency ν (ph), which occurs in range of 10^{12}-10^{13} s^{-1} (b) the wave function of the electron and (c) the probability of finding a phonon with excitation energy (*w*) large enough to accomplish the hop. The probability rate of an electron jump is given by,

$$P = \nu(ph)e^{-2\alpha R}e^{-w/kT} \qquad \text{Eq. 2-1}$$

where ξ =1/α is the decay length of localized wave function, R is the spatial distance between the two hopping sites, w is the energy difference between two states, and k is the Boltzmann constant. From the product of α and R the hopping conductivity can result from Nearest Neighbor Hopping (NNH) or Variable Range Hopping (VRH). The energy levels of a p-type semiconductor are affected by potential fluctuation. Charge carriers hop from one to another site with the assistance of a phonon. The most probable form of hopping is between

nearest neighbor atoms and is designated NNH. The temperature dependence of conductivity due to NNH is similar to that of thermal activation, where the magnitude of activation energy corresponds to the potential fluctuation. They have similar temperature dependence (i.e., the characteristic exponent (*"p"*=1) though the conduction mechanism is different. Depending on the energy of the carrier, it can migrate from one site to another site at various distances, and the resulting conductivity will deviate from NNH to VRH. The NNH conduction is expected if $\alpha R_o >> 1$ where R_o is the average distance to the nearest neighbor. If $\alpha R_o \leq 1$, VRH is expected. The hopping distance R increases with decreasing temperature[5]; as a result, NNH is expected to dominate at higher temperatures and VRH at lower temperatures. The hopping mechanism of electrical conduction corresponds to low mobility as the carrier jumps are associated with a weak overlap of the wave functions. As a result, the conductivity has an exponential dependence with temperature[44].

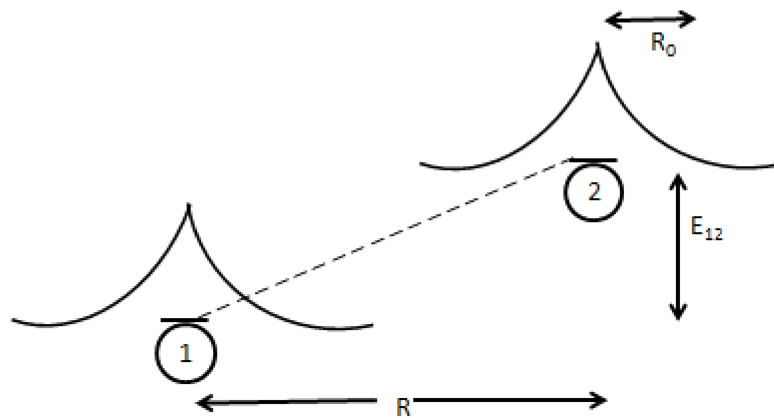

Figure 2-1. Hopping between the two localized states separated by distance R and energy E_{12}, and R_0 is the localization length[33]

Figure 2-1 shows the carrier hopping between the two states separated by the distance R and energy E_{12}.

Using Einstein's relation,

$$\text{Mobility, } \mu = \frac{eD}{kT} \qquad \text{Eq. 2-2}$$

where, $$\mu = \frac{PR^2}{6}\,. \qquad \text{Eq. 2-3}$$

The conductivity can be written as,

$$\sigma = (1/6)e^2PR^2\,N(E_F). \qquad \text{Eq. 2-4}$$

Here $N(E_F)$ is the DOS at Fermi level and $N(E_F)kT$ is the number of charge carriers that are involved in the electrical conduction. Combining with Eq. 2-1, the conductivity can be written as,

$$\sigma = (1/6)e^2R^2\nu_{ph}\,N(E_F)exp(-2\alpha R)exp(-W/kT) \qquad \text{Eq. 2-5}$$

With a decrease in temperature, the number and energy of phonons decreases and more energetic phonon-assisted hops become less favorable. Carriers will try to hop larger distances to get to sites that lie energetically closer than the nearest neighbors, resulting in a variable range for the hopping distance between traps. The exponential term $exp(-2\alpha R - W/kT)$ will not have its maximum value for the nearest neighbor. Mott used an optimization procedure to get the most probable hopping distance. If the DOS is expressed in units of volume per unit energy $N(W)$, then the possible number of states within the ΔW in a distance R from particular atom is given by, $\left(\frac{4\pi}{3}\right)R^3N(W)W$. The charge carrier can leave its original site if there exists at least one vacancy or site for its hop, and in such case the average energy spacing between the states in the vicinity of the Fermi level is,

$$W = \left(\frac{3}{4\pi}\right)\frac{1}{R^3N(E_F)} \qquad \text{Eq. 2-6}$$

And, the jump probability is,

$$P = \nu_{ph} \exp(-2\alpha R - \frac{3}{4\pi R^3\, N(E_F)kT}) \qquad \text{Eq. 2-7}$$

The most probable jump distance is found by minimizing the exponent as a function of R given by,

$$R = \{\frac{9}{8\pi\alpha\, N(E_F)kT}\}^{0.25} \qquad \text{Eq. 2-8}$$

The general expression for a hopping mechanism (obtained from the hopping probability) can be written as,

$$\sigma = \sigma_o e^{-\left(\frac{T_o}{T}\right)^p} \qquad \text{Eq. 2-9}$$

where, σ_o is the conductivity prefactor, T_0 is the characteristic temperature and "*p*" is a characteristic exponent that distinguishes between various conduction mechanisms. As the hopping conduction of charge carriers occurs between the localized states in the vicinity of the Fermi level (E_F), the details of DOS, in the vicinity of $E_{F,}$ is an important consideration in the determination of the temperature dependence of conductivity. Mott considered a constant DOS in the vicinity of the E_F and determined the value of *p*=1/4 for a three dimensional system.

However, Efros and Skhlovskii[44] considered the long range Coulomb interaction and found that it reduces the DOS to zero at the Fermi level, thereby creating a so-called "Coulomb gap (CG)" at low enough temperatures. This form of hopping conductivity results when an electron migrates from one site to another site leaving a positively charged vacancy. For

hopping to occur, the charge carrier must have sufficient energy to overcome this Coulomb interaction between the electron and the hole; and thus, a "Coulomb gap", defined by this interaction, appears[42]. The temperature dependence of conductivity, which can be described by Eq. 2-9, is still valid, but the characteristic exponent now becomes p=1/2 in this case.

Mott[5] neglected the long-range Coulomb interaction and assumed that the DOS was a constant at the Fermi energy. In general, the DOS, $N(E) \sim (E-E_F)^n$. For the Mott hopping conduction, n=0 and the DOS is constant, yielding an expression for the conductivity of the form of Eq. 2-9 with p=1/4. For ES conduction, n=2, and yields an expression for the conductivity of the form of Eq. 2-9 with p=1/2. For large value of n, p~1 in the Eq. 2-9 and corresponds to NNH conduction. Each of these hopping mechanisms and their range of validity will be briefly discussed below.

a) When the power p=1/ 4, the conduction mechanism is described by the Mott[5] model

$$\sigma_M = \sigma_{oM} e^{-\left(\frac{T_{oM}}{T}\right)^{\frac{1}{4}}} \qquad \text{Eq. 2-10}$$

Where T_{0M} is the Mott characteristic temperature given by,

$$T_{0M} = \frac{\beta}{kN(E_F)\xi^3} \qquad \text{Eq. 2-11}$$

Here, *$N(E_F)$* is the density of states at the vicinity of the Fermi level, *k* is the Boltzmann constant and β=18.

For the Mott theory to be valid, the charge carrier must "hop" an average distance that is considerably more than the nearest neighbor trap separation and considerably greater than the localization length "*ξ*".

Using the expression for T_{0M} as shown above, an equation for the hopping distance and hopping energy are given, respectively as[9],

$$R_{hop,M} = \frac{3}{8}(\frac{T_{0M}}{T})^{0.25} * \xi \qquad \text{Eq. 2-12}$$

And,

$$W_{hop,M} = \frac{1}{4}(kT)(\frac{T_{0M}}{T})^{0.25} \qquad \text{Eq. 2-13}$$

Correlations with the values of the hopping distance and energy obtained for samples differing in doping and H-dilution will be given in the results section of this chapter.

b) For the power p=1/2, the conductivity equation results from the Efros-Shklovskii-VRH[44] which is,

$$\sigma_{ES} = \sigma_{0ES} e^{-\left(\frac{T_{0ES}}{T}\right)^{\frac{1}{2}}} \qquad \text{Eq. 2-14}$$

Where σ_{0ES} is the prefactor and T_{0ES} is the characteristic temperature for the ES-VRH given by,

$$T_{0ES} = \frac{\beta' e^2}{k\ \varepsilon\xi} \qquad \text{Eq. 2-15}$$

with β'=2.8 and ε is the dielectric constant of the medium, ξ is the localization length[10].

For the ES theory, the average hopping distance must be greater than the nearest neighbor distance and greater than the localization length. In this case, when the Fermi energy lies in a range of energies where the states are localized, the Coulomb interaction results in a zero in the density of states at the Fermi level that leads to the formation of a Coulomb Gap (CG)[9,43]. The appearance of the CG by electron correlations can be considered the minimum energy

required for a hopping conduction process to occur between the localized states with finite energy and spatial distribution[15, 44].

c) When p=1, the conductivity can be expressed as,

$$\sigma = \sigma_o e^{-\left(\frac{T_o}{T}\right)} \qquad \text{Eq. 2-16}$$

The conduction results from hopping between nearest neighbor sites, referred to as the nearest neighbor (NNH) model[11].

2.2 Temperature Coefficient of Resistance (TCR)

The TCR is a measure of the rate at which the conductivity changes with temperature. For certain applications, such as a bolometric sensor, the TCR is a figure of merit, because an increase in the TCR correlates with an increase in the bolometric response. The nature of the TCR can be understood and described by the specific mechanisms controlling electrical conduction.

The TCR is defined as[8],

$$|TCR| = \left|\frac{1}{\sigma}\frac{d\sigma}{dT}\right| \qquad \text{Eq. 2-17}$$

where σ is the conductivity of the material at temperature T.

For a conductivity described by Eq. 2-9, the general equation connecting the TCR with the power *"p"* is given by,

$$|TCR| = \left|\frac{1}{\sigma}\frac{d\sigma}{dT}\right| = p\frac{{T_0}^p}{T^{p+1}} \qquad \text{Eq. 2-18}$$

It is sometimes convenient to write the Eq. 2-18 in the following form,

$$(\frac{T_0}{T})^p = -\frac{T}{p}TCR \qquad \text{Eq. 2-19}$$

where, the values of *p* lie between 0 and 1.

For NNH, Eq. 2-18 becomes,

$$\left|TCR_{NNH}\right| = \frac{T_0}{T^2} \qquad \text{Eq. 2-20}$$

In the case of the M-VRH, the value of p= ¼, then TCR is given by,

$$\left|TCR_M\right| = \frac{1}{4}\left(\frac{T_{oM}}{T^5}\right)^{1/4} \qquad \text{Eq. 2-21}$$

Similarly, the TCR for ES-VRH (with p=1/2) is given by,

$$\left|TCR_{ES}\right| = \frac{1}{2}\left(\frac{T_{oES}}{T^3}\right)^{1/2} \qquad \text{Eq. 2-22}$$

In terms of the conductivity and its prefactor $\boldsymbol{\sigma}_{0,}$ the general TCR can be expressed as,

$$TCR = p\frac{1}{T}(ln\sigma_0 - ln\sigma) = p\frac{1}{T}(ln(\rho\sigma_0) \qquad \text{Eq. 2-23}$$

This shows that, the TCR is directly proportional to the resistivity. In the discussion section, the experimental results from the reprentative samples will be discussed with TCR values obtained by numerical differentiation of the conductivity data.

2.3 Sample Information

The sample and device structure for the electrical measurements are given below in Figure 2-2 and Figure 2-3 respectively.

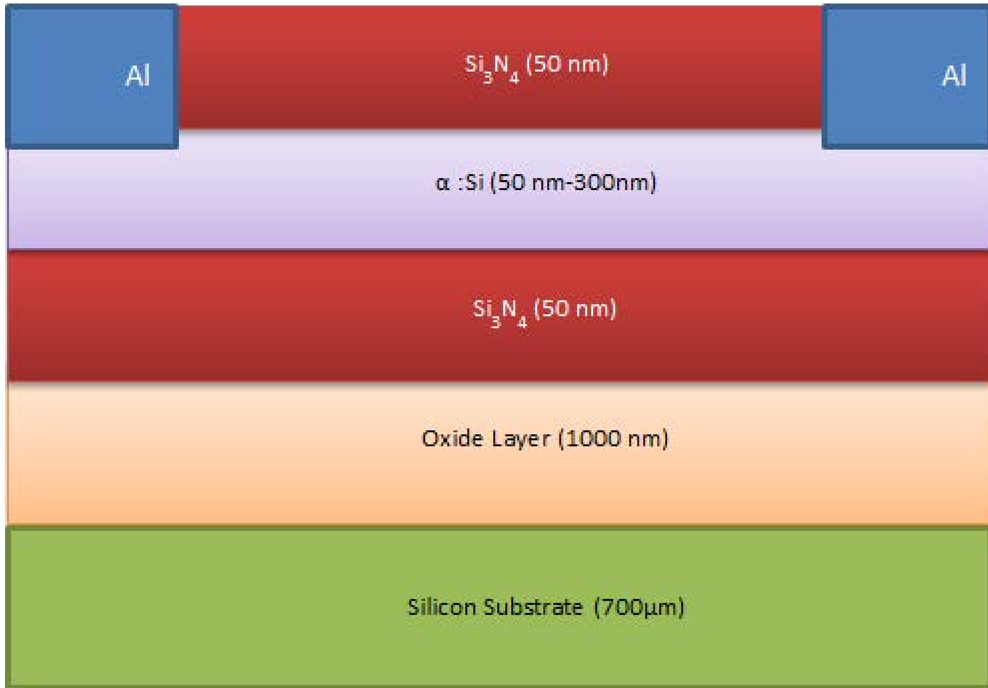

Figure 2-2. Sample structure showing different insulating layers and the sandwiched active material a-Si:H

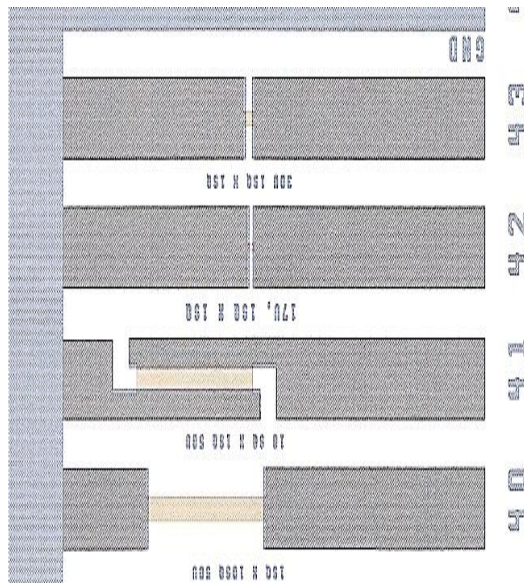

Figure 2-3. Schematic of device structure fabricated at L-3 Communications

Figure 2-3 shows the sample test structures developed at L-3 Communications for electrical measurements. The amorphous silicon thin films were grown by PECVD using capacitively-coupled 13.56 MHz plasma with the substrate on the ground electrode. The growth temperatures for the samples studied were 275 ºC and 365 ºC. The source gases are silane (SiH_4) and hydrogen in Argon. The films were deposited on Si wafers with an insulating SiO_2 layer and a silicon nitride film Si_3H_4 layer as shown in Figure 2-2. The thickness of the a-Si: H layer range from approximately 500 Å to 3000 Å. The films were doped p-type by using boron trichloride (BCl_3) as a dopant precursor to incorporate boron in the thin films. The doping ratio is defined as "r" = $[BCl_3]/[SiH_4]$, and H-dilution as "R_H"=$[H_2]/[SiH_4]$.

Standard photolithography techniques were used to prepare two, three and four terminal test structures. Aluminum pads shown as "Al" are the contacts made for electrical measurements. Samples from the wafer were die-attached onto ceramic carriers and wire-bonded for temperature dependent electrical measurements.

2.4 Electrical Conductivity and TCR Measurements

Resistivity measurements were obtained by recording the current–voltage (I-V) characteristics, determining the Ohmic region, and extracting the resistance. Four terminal measurements were also performed by the Van der Pauw technique to cross check the resistivity obtained by two terminal measurements. When measuring high resistance films, an electronic card with high impedance buffers ($R_{buffer} >> R_{sample}$) was used so that measurement electronics did not affect the measured voltages. The block diagram used for Van der Pauw resistivity and Hall Effect measurements is shown in Figure 2-4. The equipment consists of a Keithley 6221 current source, 2182A nanovoltmeter, 6485 picoammeter, 7001 switch system

with 7065 hall card, and electromagnet including power supply. The setup can be modified or rearranged depending upon the resistance of the sample to measure, as it has the capacity to measure either high or low resistivity materials. The conductivity was measured using a sufficient wait time (15 minutes) after reaching the set temperature to make sure that the sample was in thermal equilibrium with the cold finger of the cryostat at a particular temperature.

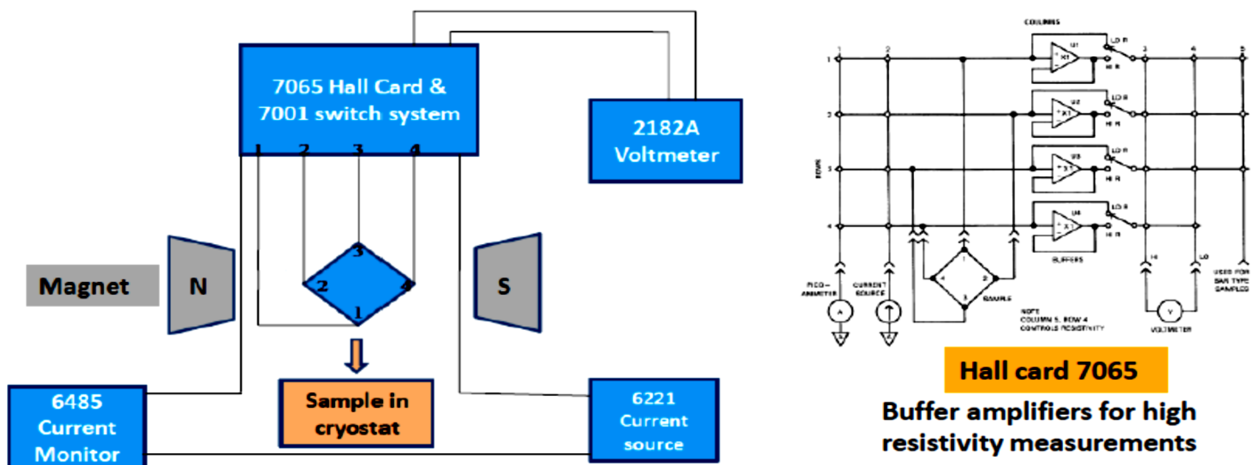

Figure 2-4. Block diagram of equipment used to measure Van der Pauw resistivity, two terminal resistivity and Hall Effect.

Figure 2-5. Resistivity and Hall Effect measurement Equipment (photograph).

Resistivity can be also be determined by using the Van der Pauw technique[45,46]. This consists of four small Ohmic contacts located about the perimeter of a homogeneous and contiguous sample. Eight voltage measurements are made about the perimeter of the sample to account for any offsets. Van der Pauw showed that the sheet resistance of samples with arbitrary shapes can be determined from resistances R_a and R_b by using the expression,

$$e^{-\pi R_a / R_S} + e^{-\pi R_b / R_S} = 1 \qquad \text{Eq. 2-24}$$

The corresponding resistivity is determined by $\rho = R_S \times d$, where d is the thickness of the sample.

2.5 Results and Discussion

The conductivity versus temperature plot for samples representing a wide range of doping and H-dilution prepared at the growth temperature of 365 °C is shown in Figure 2-6.

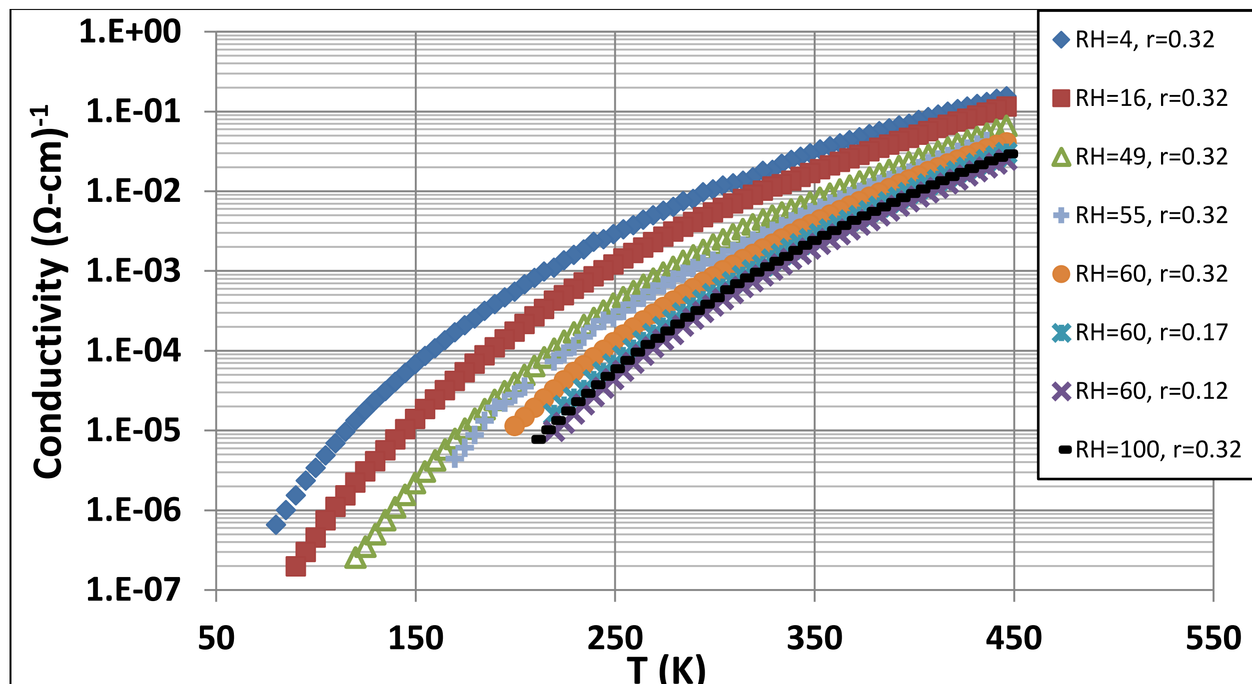

Figure 2-6. Temperature dependent conductivity of various samples differing in boron doping and H-dilution

The results shown indicate that the conductivity increases with the boron doping and decreases with increasing hydrogen (R_H). Samples with the lowest R_H and highest "r" have the highest conductivity. To better illustrate the effect of hydrogen on conductivity is shown in the Figure 2-7.

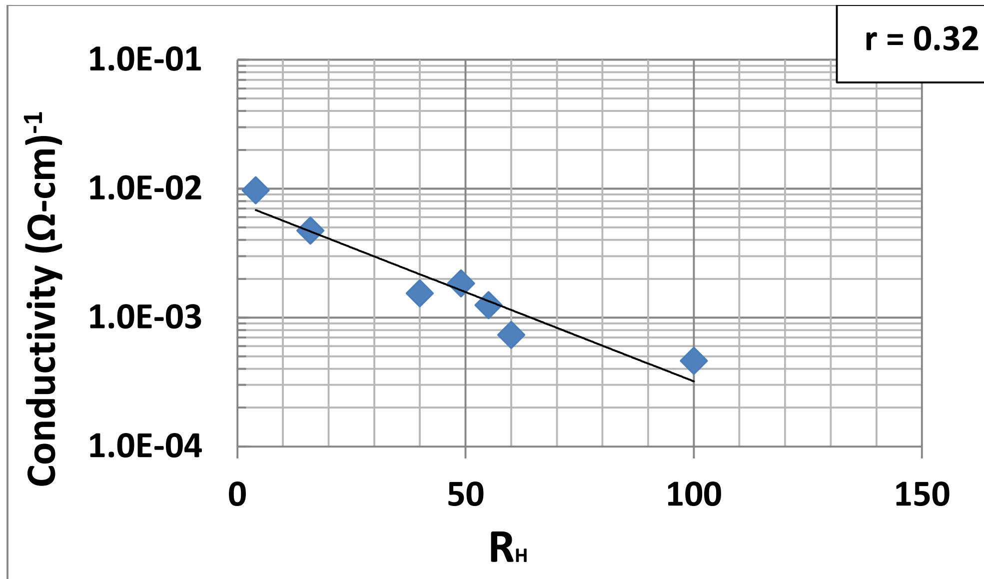

Figure 2-7. Room temperature conductivity vs. R_H for fixed boron doping r = 0.32 (highest doping)

Figure 2-7 illustrates the decrease of conductivity with the increase of H-dilution for the highest doping ratio. More about the bonding energy between different elements will be discussed shortly.

Figure 2-8 shows the experimental results obtained for samples having two different boron doping ratios (r=0.17 and 0.32), two different dilutions (R_H=40, and 55) and thickness close to 1000 Å.

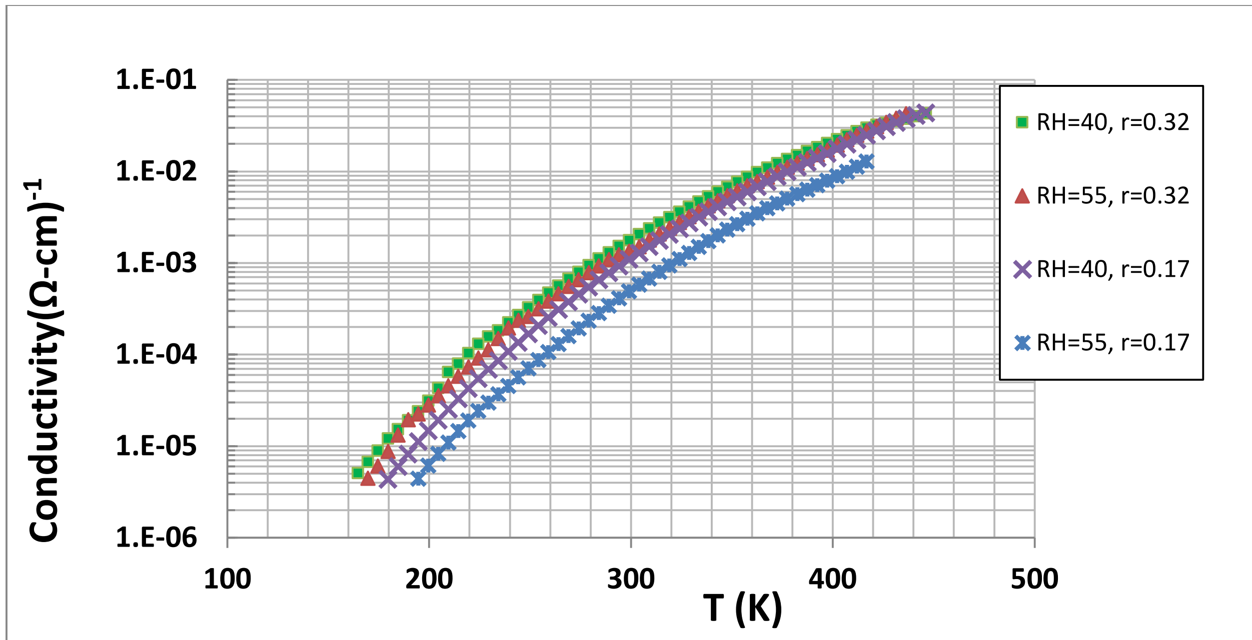

Figure 2-8. Conductivity of a-Si:H thin film (~1000 Å thick) for different H-dilution (R_H) and boron doping ratio ®.

Figure 2-8 clearly shows that for a fixed dilution if the doping is increased the conductivity increases. Furthermore, for a fixed doping, if the R_H is increased the conductivity decreases. The room temperature resistivity values for these samples are in the Table 3.

These general features due to hydrogen and boron incorporation can be described as follows: The mobility gap of a-Si increases with the increase of R_H due to the passivation of dangling bonds[47,48,49], which results in a decrease in conductivity. The mobility gap increase results from the introduction of hydrogen due to the formation of the higher bonding energy of the Si-H bond over that of the weaker Si-Si bonds[47]. This effect is evident in a-Si grown by Glow discharge[50](P. J. Zanzucchi et al) and reactively sputtered[51] (B. von Roedern et al) techniques and should be expected on PECVD-grown a-Si:H.

With the addition of boron there is an increase of conductivity due either to the activation of the boron substitutional acceptor in the a-Si:H matrix or by the “gettering’” of hydrogen by boron, leading to the reduction of hydrogen available to passivate the dangling bonds. An increase in the number of Si-B bonding results in the increase of electrical conductivity due to reduction of the gap, because the Si-B bonding energy (2.1 eV) is smaller than Si-Si (2.2 eV) and Si-H (3.4 eV) bonding energies[52,53].

Figure 2-9 shows the experimental results of the samples with fixed H-dilution (R_H =60) of three different levels of boron doping (r=0.12, 0.17, and 0.32) where the conductivity vs. temperature is plotted.

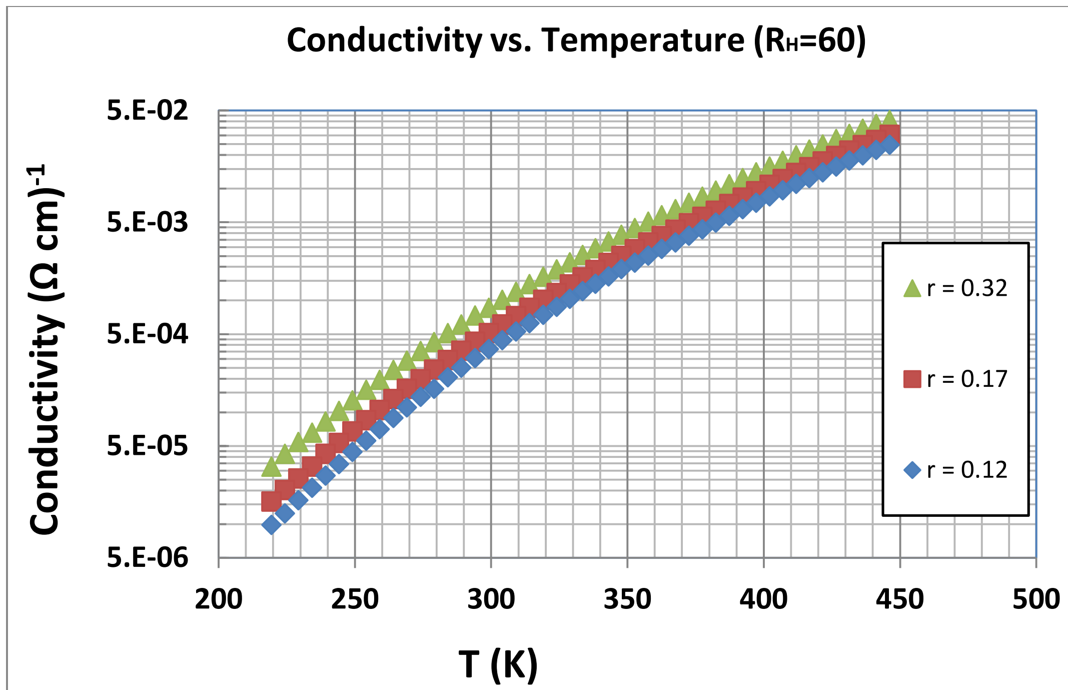

Figure 2-9. Conductivity of a-Si:H thin film (~500 Å thick) for fixed R_H and different boron doping

As mentioned earlier, the graph clearly shows that the conductivity increases with the increase of the boron concentration. To determine which conductivity mechanism dominates in these samples, the log of the conductivity versus T $^{-¼}$, $T^{-1/2}$, and T^{-1} has been plotted in Figure 2-10.

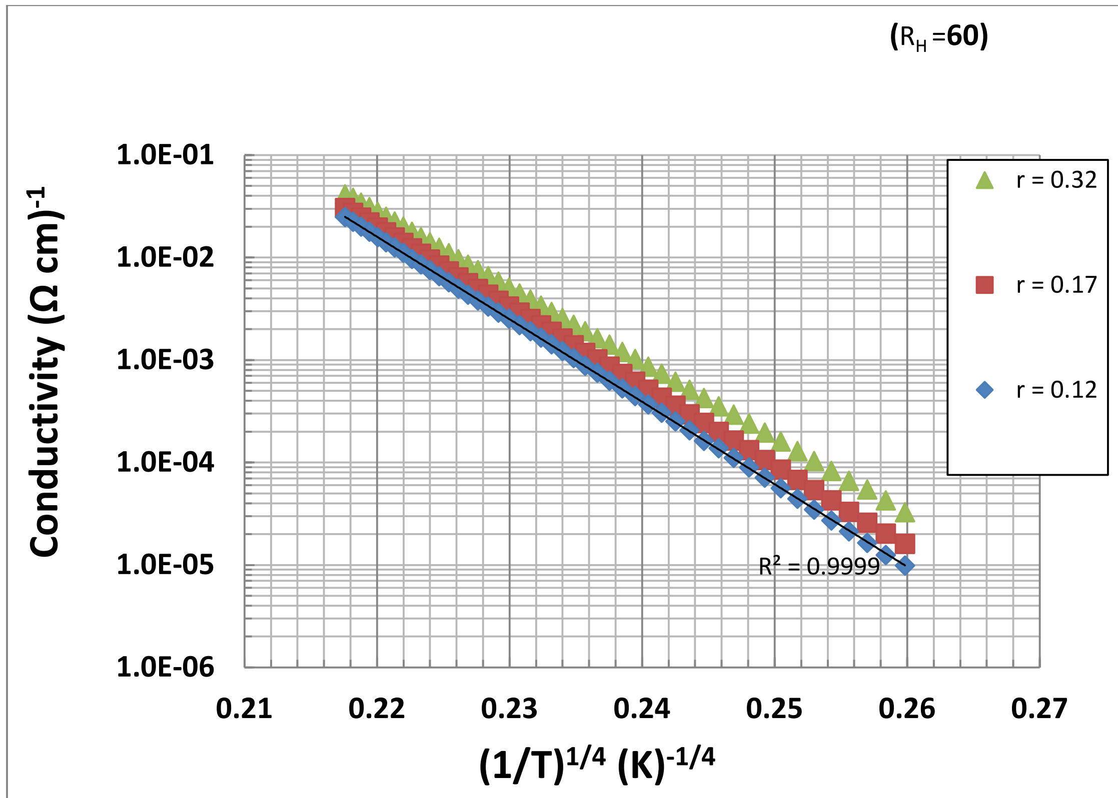

(a)

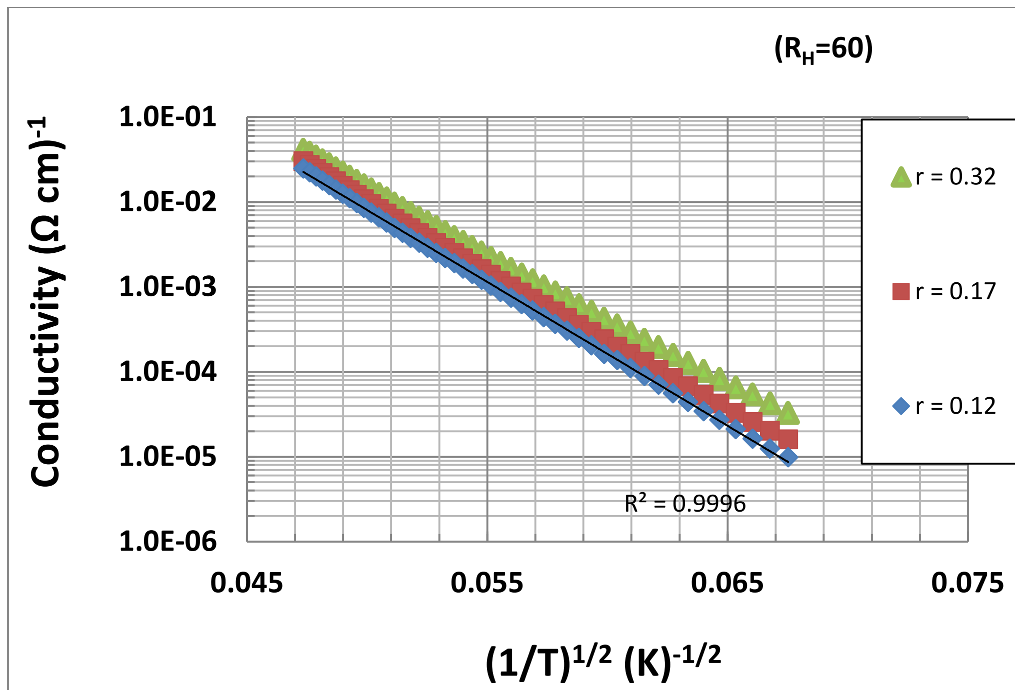

(b)

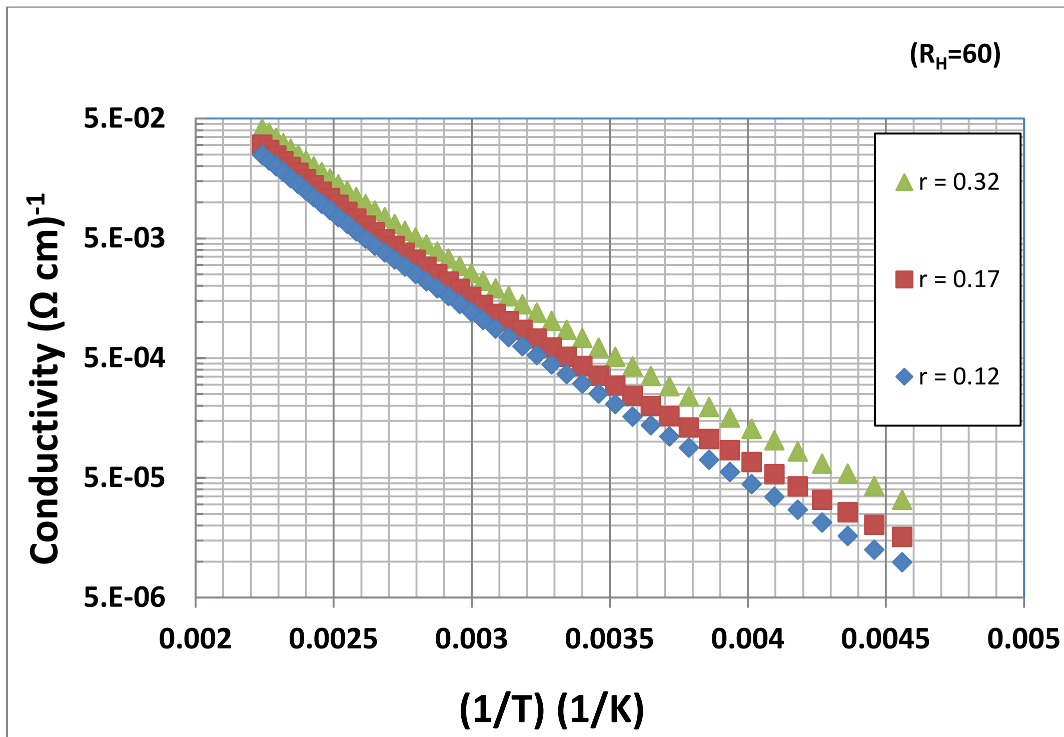

(c)

Figure 2-10. (a) Log conductivity vs. $T^{-1/4}$ and (b) Log conductivity vs. $T^{-1/2}$ © Log conductivity vs. T^{-1}

In order to determine the conduction mechanism, as shown in Figure 2-10, the Log conductivity vs. $T^{-1/4}$ and $T^{-1/2}$ are fit by the Mott and ES VRH conduction models. It is seen that the Mott expression provides only a slightly better fit to the data points, as evidenced by the higher R^2 value. From the conductivity vs. $T^{-1/2}$ the R^2 value is 0.9996 and from conductivity vs. $T^{-1/4}$ the R^2 value is 0.9999. However, the difference in R^2 values is small, making it difficult to distinguish the best between the Mott and ES VRH models.

In order to better delineate which conductivity mechanism dominates, a Resistance Curve Derivative Analysis (RCDA)[54, 9] method was performed on the data shown in Figure 2-11. This method allows one to extract the power value "*p*" directly from the analysis and thus the transport mechanism. In the RCDA method, the log of the conductivity data versus temperature is numerically differentiated, and the quantity "*w*", is determined.

where ,

$$w = \frac{d\ (\log \sigma)}{d\ (logT)} \quad \text{Eq. 2-25}$$

From Eq. 2-9, the quantity "*w*" can be expressed as,

$$w = p\left(\frac{T_0}{T}\right)^p \quad \text{Eq. 2-26}$$

The expression can be written in the straight line form as,

$$\log w \ = \log p(T_0)^p \ - p\log T \quad \text{Eq. 2-27}$$

comparing with straight line equation y = mx+b, the value *"p"* is obtained from the slope and the y- intercept value "*A*" can be used to get the characteristic temperature by using the equation,

$$T_0 = \left(\frac{10^A}{p}\right)^{\frac{1}{p}}$$ Eq. 2-28

Recalling the TCR relation with *"p"* and combining with the "*w*" we obtain a simple expression which, relates TCR and "w" with temperature.

$$TCR = \frac{w}{T}$$ Eq. 2-29

Figure 2-11 shows the plot of log *w* vs. log T for a representative sample.

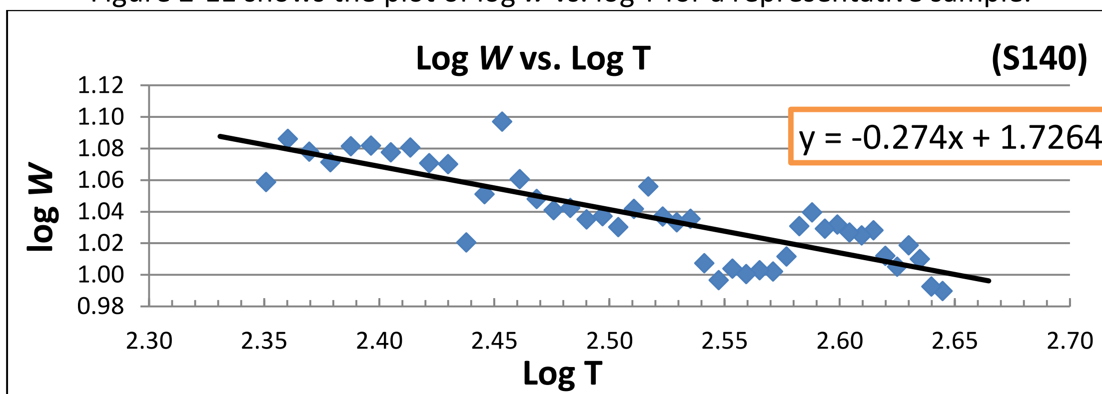

Figure 2-11. Illustration of the RCDA method

By the RCDA method, for S-140 (r=0.12) the "T_0"and the *"p"* values are 1.1x10^9 K and 0.274 respectively. Similarly the "T_0" and *"p"* values for S-143 (r=0.17) are obtained as 1.0 x10^9 K and 0.249 respectively and for the S-114 (r=0.32) "T_0" is 8.2 x10^8 K and *"p"* is 0.249. Given below (Figure 2-12) are all three samples with R_H=60 having three different boron levels. The derived *"p"* values are also indicated by the slope of the linear fit.

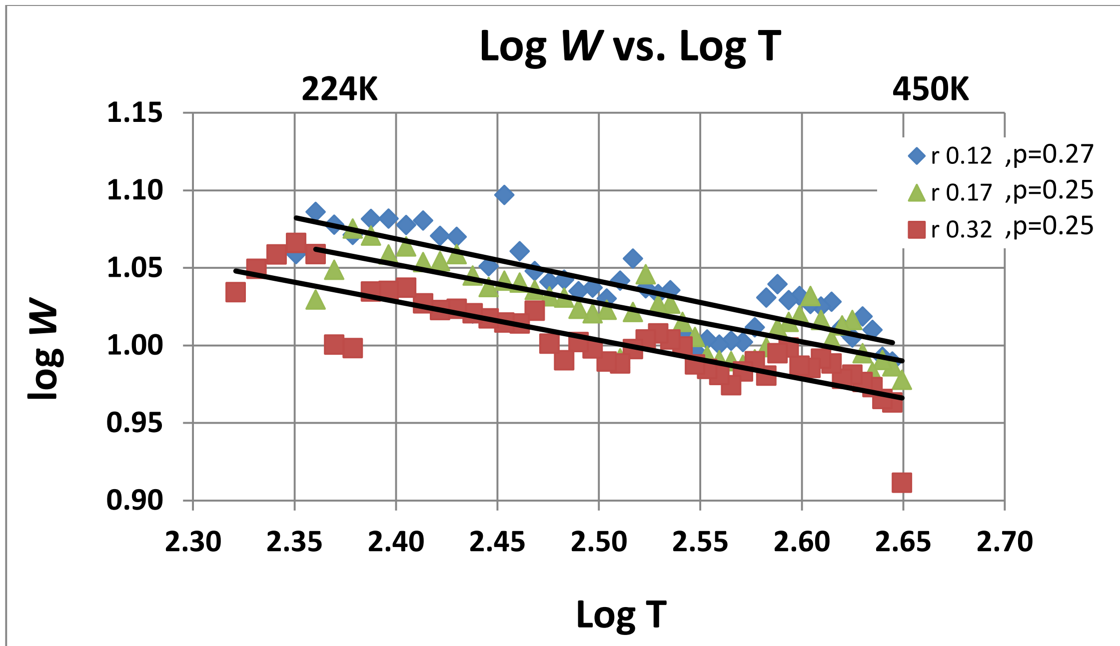

Figure 2-12. RCDA of a-Si:H samples for fixed R_H and various doping levels
Since all values of *"p"* are close to or equal to 0.25, the dominant conduction mechanism is the Mott-VRH in these samples. From Eq. 2-26 and Eq. 2-28 the TCR is a function of *"p"* as well.

As mentioned earlier, the TCR is determined by taking the derivative of conductivity data and dividing by the conductivity. For the set of samples the numerical derivative of the experimental values of the conductivity with respect to the temperature was performed and compared to the predictions of the Mott-TCR model in Figure 2-13. There is a good agreement between the experimental results and the model, further validating the Mott mechanism of conduction for these samples.

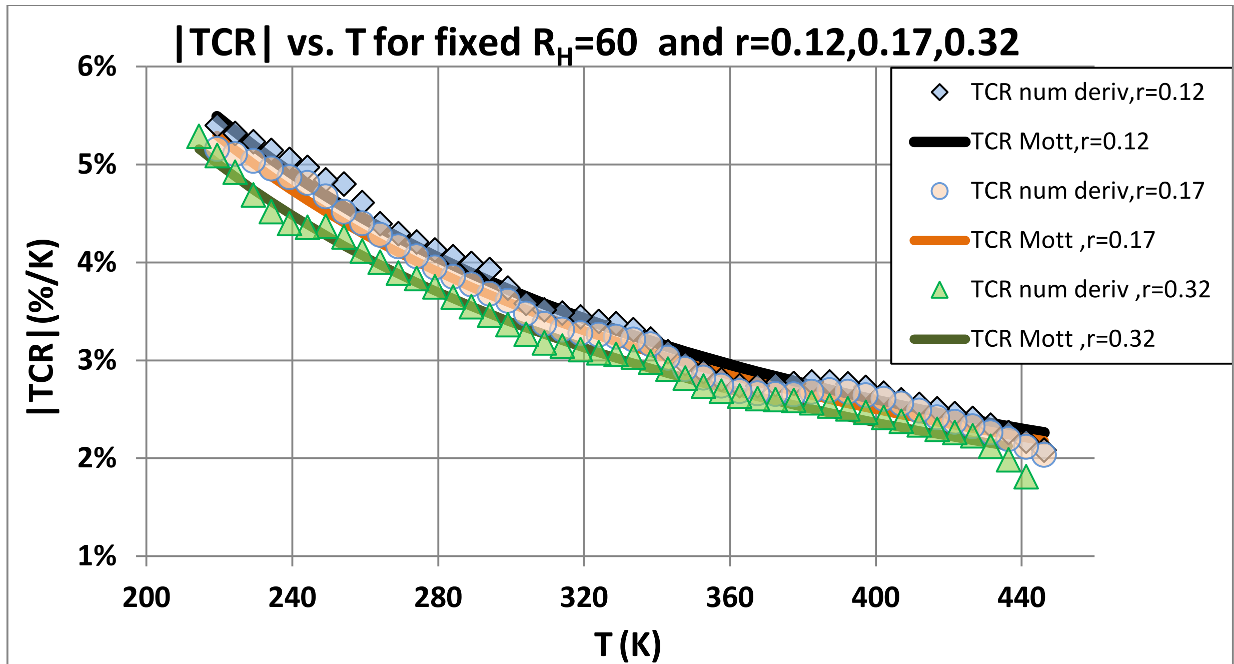

Figure 2-13. TCR of the samples with fixed R_H and three different “r” values

Table 1 shows the Mott- parameters along with the TCR_Mott values at room temperature for the set of samples with fixed R_H and varying boron doping ratios.

Table 1. Parameters determined by Mott-fitting of conductivity and TCR data at room temperature

ID	[“r”]	[R_H]	Thickness(Å)	RT Resistivity (Ω-cm)	σ_{0M} $(\Omega\ cm)^{-1}$	To(K)	|TCR_Mott|	Value of “*p*”
S140	0.12	60	523	3267	8.33E+15	$1.10\text{x}10^9$	3.81	0.274
S143	0.17	60	521	2336	2.37E+15	$1.02\ \text{x}10^9$	3.68	0.249
S114	0.32	60	519	1360	4.10E+14	$8.20\ \text{x}10^8$	3.48	0.249

The table indicates that, with an increase of boron doping for fixed R_H, the TCR decrease as the Mott parameter decreases. Once the analysis has determined the conduction mechanism, the TCR can be predicted and compared to the TCR calculated from the temperature-dependent conductivity data. That the values of *“p”* for various doping values are close to ¼ indicates that the mechanism is according to the Mott-VRH. Comparing the values obtained by RCDA method within the Table 1, it can be clearly seen that the *“p”* values are in excellent

agreement and the power values are very close to ¼ in this set of samples, confirming that the conduction mechanism is the M-VRH in the temperature range studied (~200 K-450 K). Further, the TCR values by numerical differentiation and the TCR_Mott are in reasonable agreement as shown in the Figure 2-13. At low temperatures, the conductivity is seen to deviate from M-VRH as shown in Figure 2-14, for a low dilution, highly doped sample, indeed indicate that the conductivity deviates from solely M-VRH conductivity. The conductivity can be described in terms of a combination of M-VRH and ES-VRH, where the total conductivity is given by $\sigma = \sigma_M + \sigma_{ES}$.

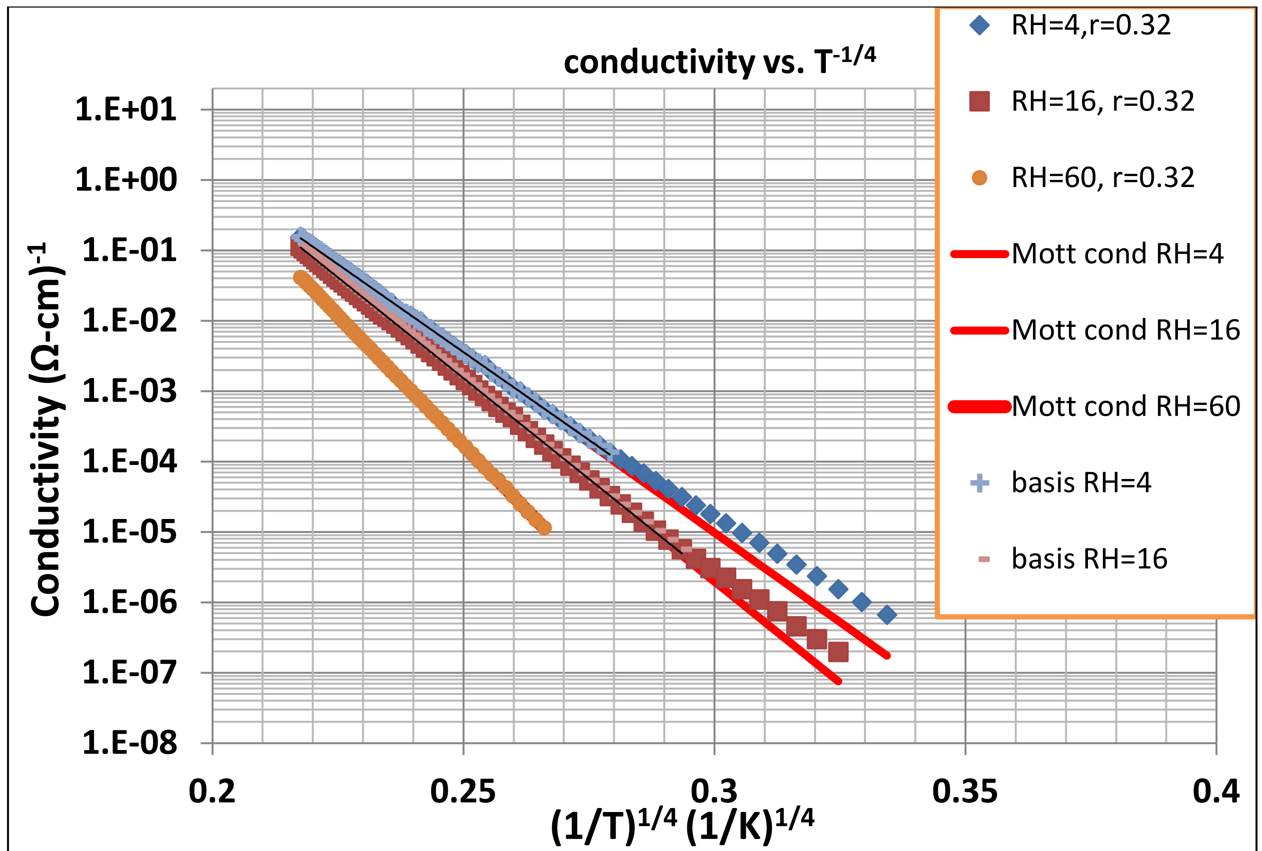

Figure 2-14. Conductivity vs. $T^{-1/4}$

The results of the analysis are shown in Figure 2-15 and Figure 2-16. Each shows contributions from both the M-VRH and the ES-VRH, as represented by the blue line and the black lines respectively. The red line is the sum of the Mott and the ES conductivities and shows the fit to the data points. The derived conductivity parameters are tabulated in Table 2.

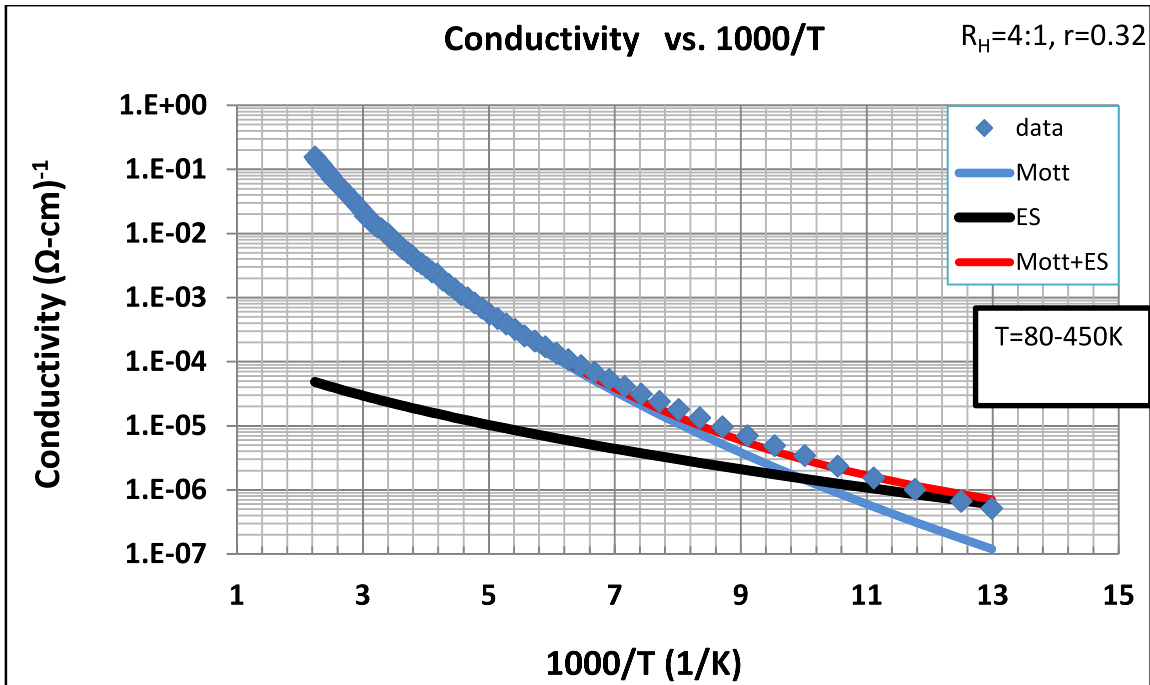

Figure 2-15. Temperature dependent conductivity for R_H=4, showing the contributions of Mott and ES conductivity and the fit to the experimental results.

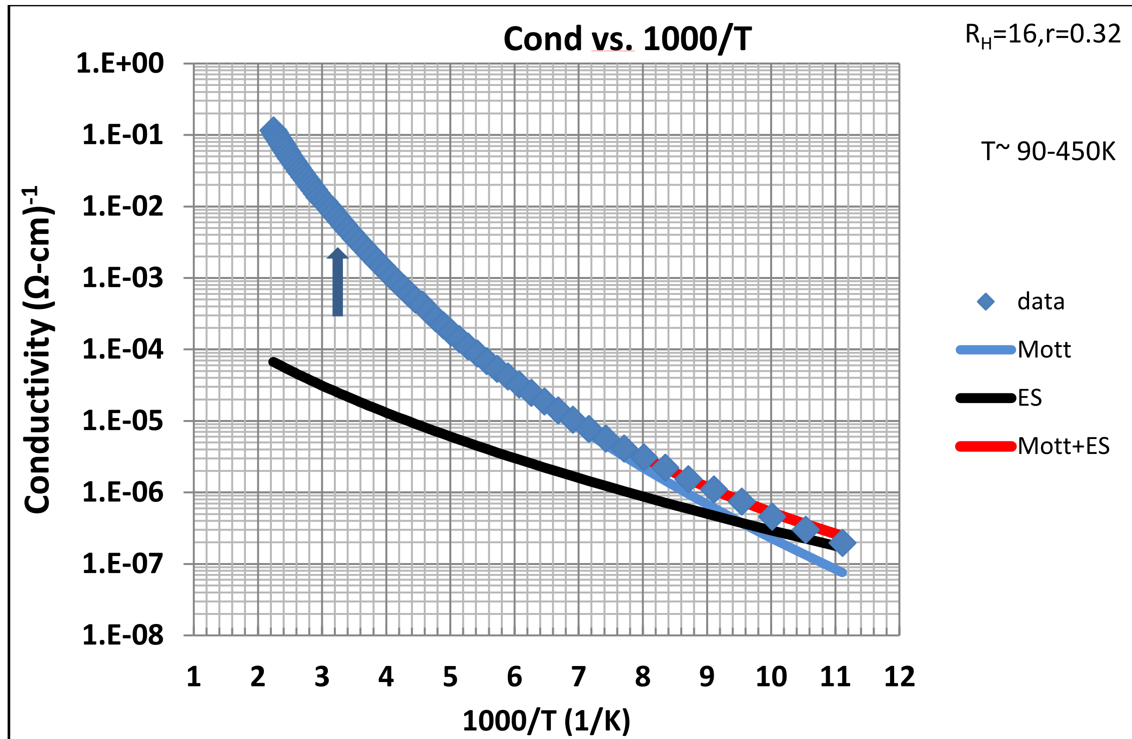

Figure 2-16. Temperature dependent conductivity for R_H 16, showing the composite of Mott and ES conductivity fits the data.

Table 2. Conductivity prefactors and characteristic temperatures for the Mott and Efros-Shklovskii mechanisms

ID	["r"]	[R_H]	RT resistivity (Ω-cm)	σ_{0M} (Ω-cm)$^{-1}$	σ_{0ES} (Ω-cm)$^{-1}$	T_{0M} (K)	T_{0ES} (K)
MMC5	0.32	4	103	1.71×10^{10}	0.0011	1.87×10^{8}	4360
MMC2	0.32	16	211	3.10×10^{11}	0.0088	3.04×10^{8}	10600

In Figure 2-17 for the sample with the lowest R_H, the TCR and conductivity are plotted with respect to temperature. It can be seen that for an increase in temperature the conductivity increases and the TCR decreases, as expected. The fitted TCR by the solid line shows that the composite TCR (Eq. 2-30) fits with the numerically obtained values by the derivative of conductivity data.

The numerical derivative provides a more sensitive measure of the contributions to the conductivity than the conductivity alone. Thus, fitting the TCR and the conductivity data assures the most accurate determination of the parameters that best describe the experimental results. Table 2 shows the related conductivity prefactors and characteristic temperatures for the set of samples having fixed boron doping and R_H=4, and 16.

It can be seen from the diagrams above that, there is a contribution of both the Mott and the ES to the conductivity, which is represented by the red curve. For the TCR data as well, there is a contribution of the ES at low temperatures and need to account it to add in to the TCR_Mott by the formula,

$$|TCR|_{tot} = \frac{\sigma_M}{\sigma_M + \sigma_{ES}}|TCR|_M + \frac{\sigma_{ES}}{\sigma_M + \sigma_{ES}}|TCR|_{ES} \qquad \text{Eq. 2-30}$$

An example of this approach is shown in Figure 2-17, which has wide coverage of temperature on measurement of conductivity.

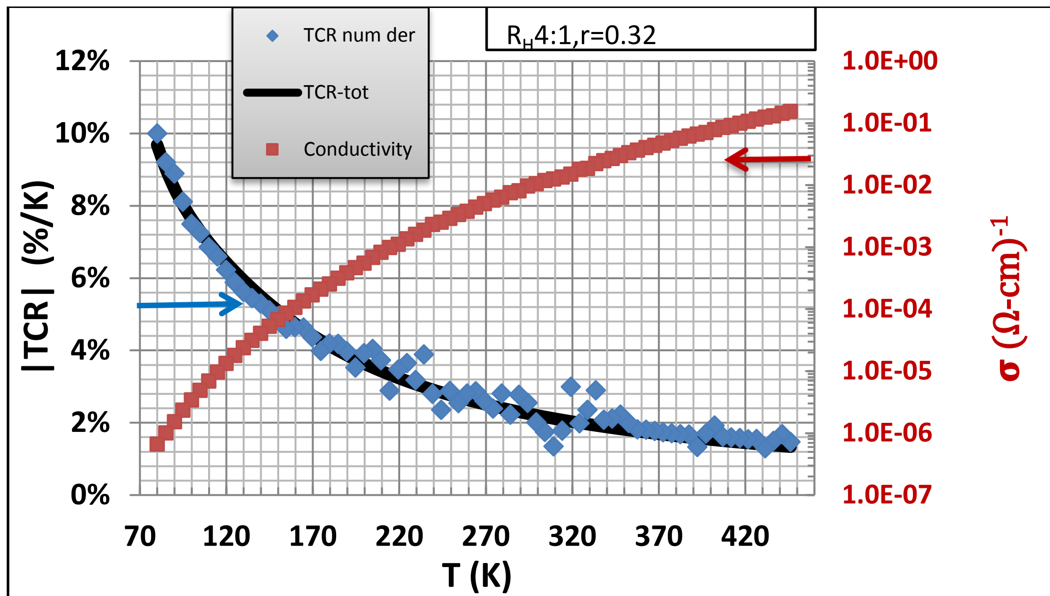

Figure 2-17. Conductivity and TCR vs. Temperature, showing fit to TCR obtained from experimental conductivity

As indicated in Figure 2-17, the numerically obtained TCR by conductivity data (red squares) and the TCR fit according to the Eq. 2-30 are in excellent agreement. Hence, the data is best described by combination of the Mott and the ES mechanisms. In the following section, a detail presentation of the several conduction mechanisms associated TCR is presented.

The Figure 2-18 represents the compilation of the TCR results along with the sample having highest H-dilution. The solid lines are the fit according to Eq. 2-30 to the numerically derived TCR data. The highest dilution sample, which solely follows the Mott fit.

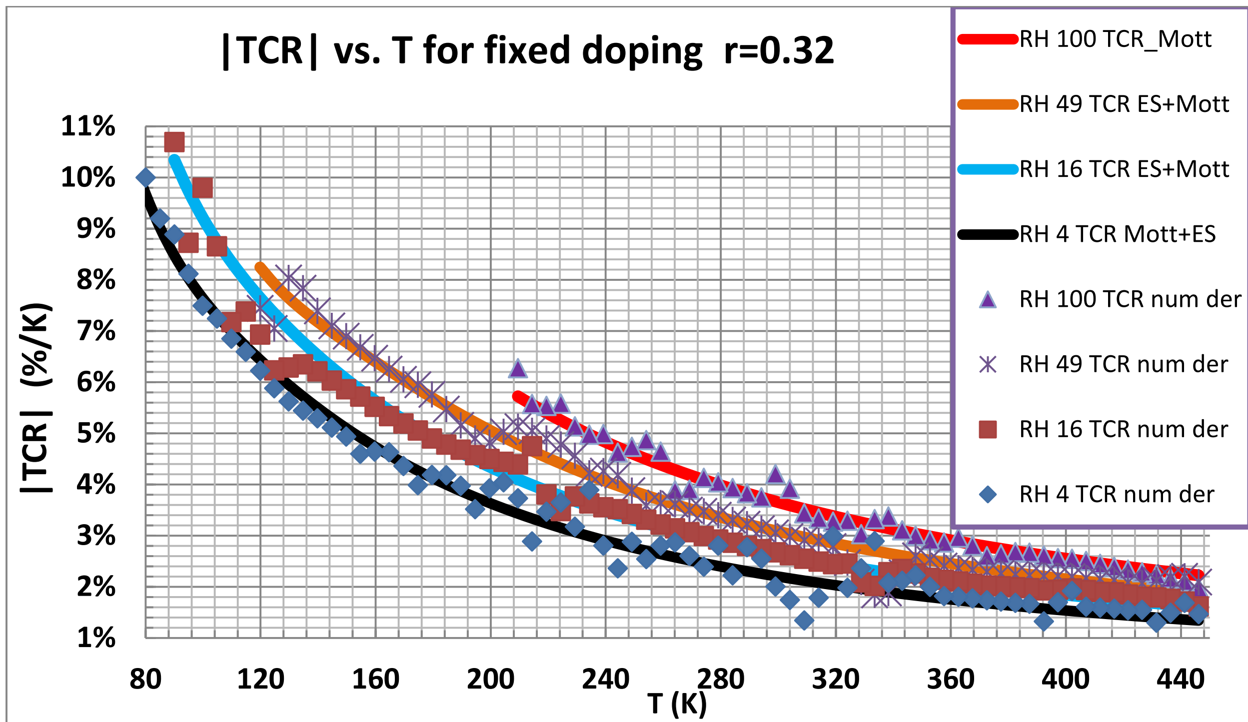

Figure 2-18. TCR data and the TCR fit for samples having fixed r and varying R_H

Hence, Figure 2-18 shows that the combination of the TCR_Mott and the TCR_ES best describe the TCR data obtained by experiment. The highest dilution sample shown is described by TCR_Mott alone. In addition, it is clear from the figure that, higher value of R_H gives higher

TCR, as expected. The Mott parameters are presented in Table 3 along with the TCR_Mott parameters at room temperature (RT).

The determined parameters are mentioned in the Table 2 for Mott and Efros parameters. As the conductivity is controlled by different mechanism in different temperature regimes, a comparison of TCR_Mott with TCR_ES using Eq. 2-21 and Eq. 2-22 can be made. If the T_{oM} (1E8 K) and T_{oES} (1E4 K) values are considered then the ratios of TCR_Mott to TCR_ES is close to 2 at room temperature. It can be concluded that the TCR_ES will be less by a factor of 2 and it will be less compare to TCR_Mott in the range of temperature studied 80-450 K. Mott VRH is the dominant conduction mechanism for the temperature range. Hence, from the material prospective follow of Mott mechanism is better than ES mechanism for the devices like microbolometer from the performance point of view.

For the fixed boron doping ratio (r=0.32) the TCR values at RT are plotted against R_H and boron doping and shown in Figure 2-19.

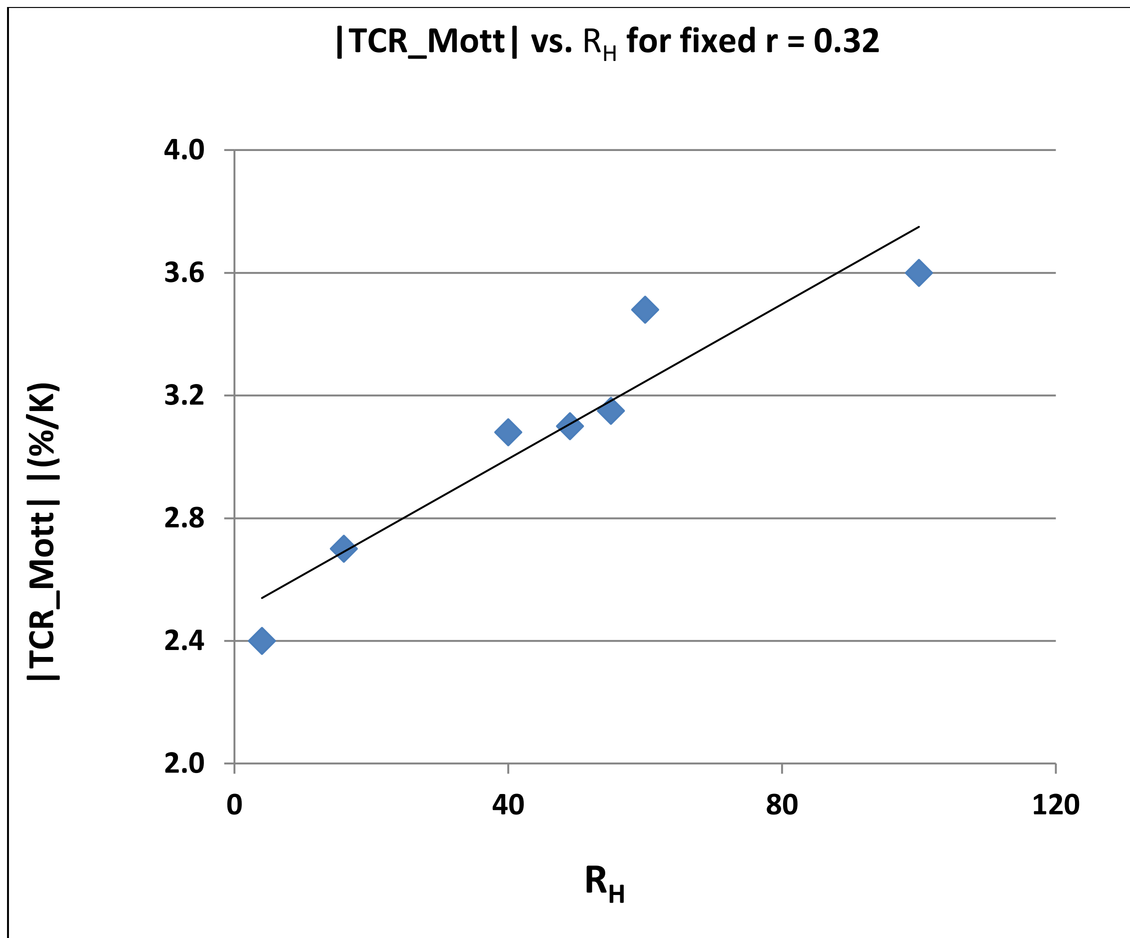

(a)

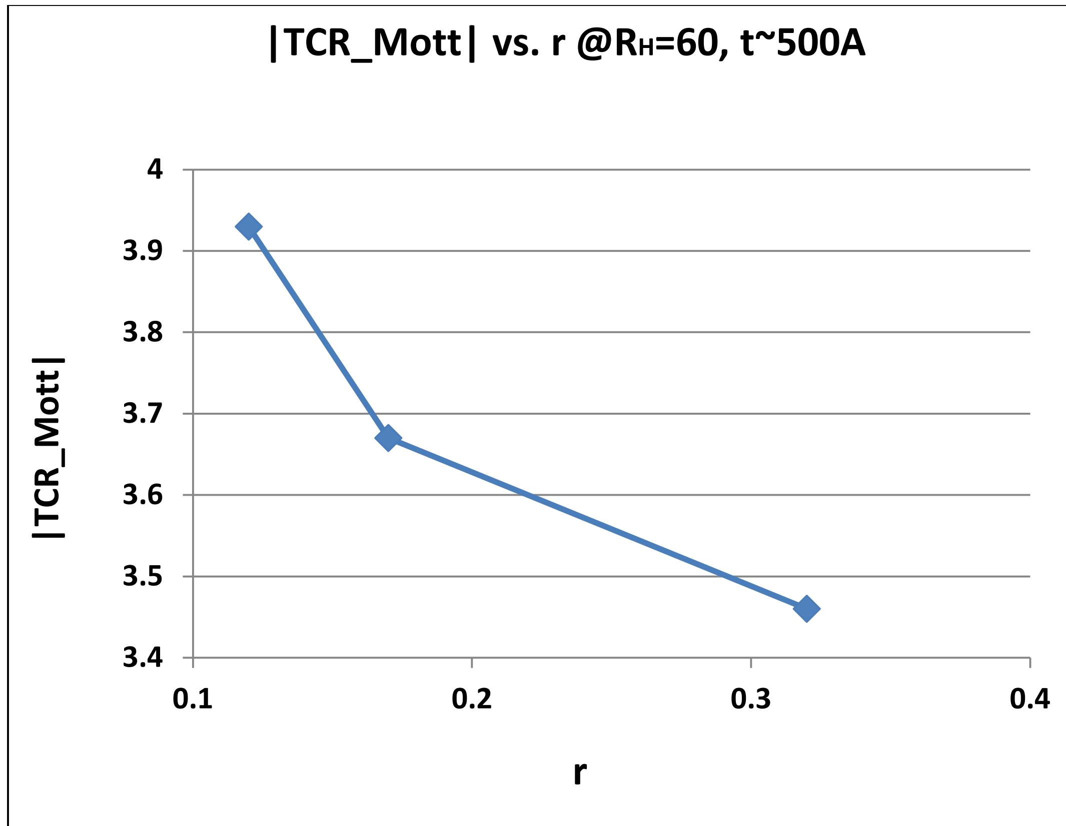

(b)

Figure 2-19. (a) TCR_Mott vs. R_H at fixed "r"=0.32 and (b) TCR_Mott vs. "r" at fixed R_H=60 and (b) different boron doping "r" (0.12, 0.17, 0.32)

Figure 2-19 shows a linear relationship between TCR_Mott and R_H, which is due to the increase of resistivity with the increase of R_H. Additionally, TCR_Mott vs. "r" shows the inverse behavior, as the resistivity decreases with an increase of the boron doping. This implies that there is a competition between boron and silicon to capture hydrogen.

Figure 2-20 shows the expected increase in the TCR_Mott with an increase of resistivity for fixed "r" and indicates that the TCR linearly increases with an increase in resistivity.

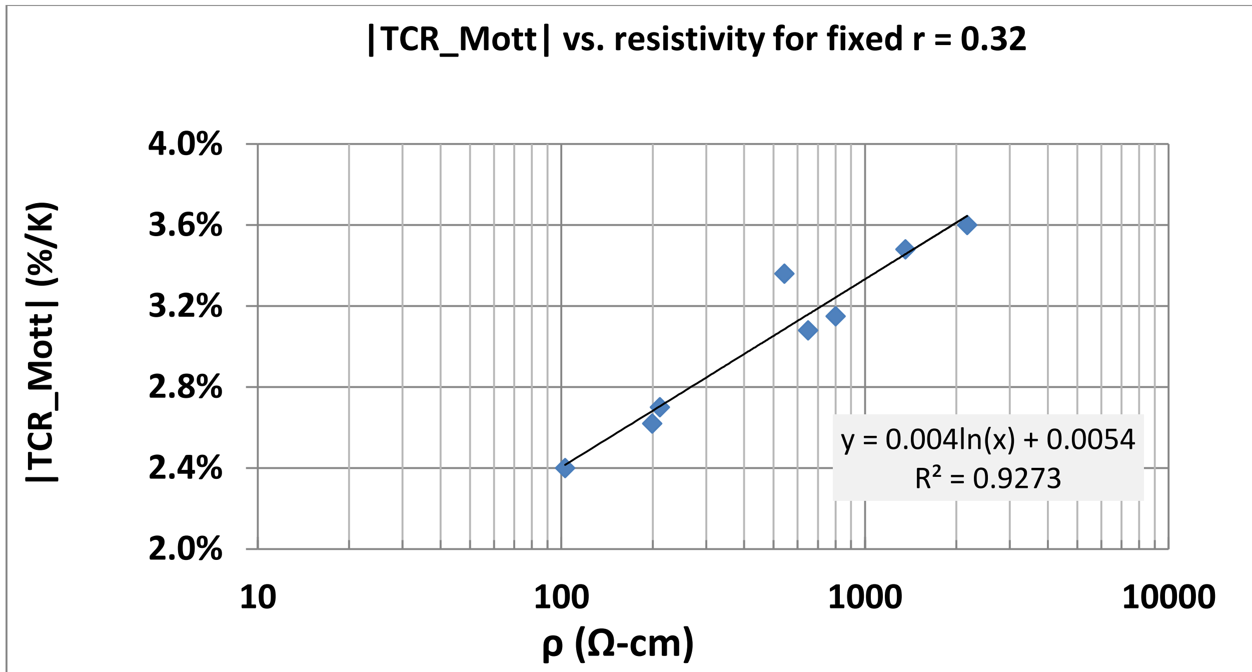

Figure 2-20. TCR_Mott vs. resistivity for fixed boron doping (highest doping r = 0.32 in the family of samples), indicating a trend of increase in TCR as the resistivity increases due to the increase in R_H.

Figure 2-21 shows the plot for TCR vs. Log ρ for different samples with various doping and dilutions and, as indicated by Eq. 2-23, shows that TCR is proportional to the log of resistivity.

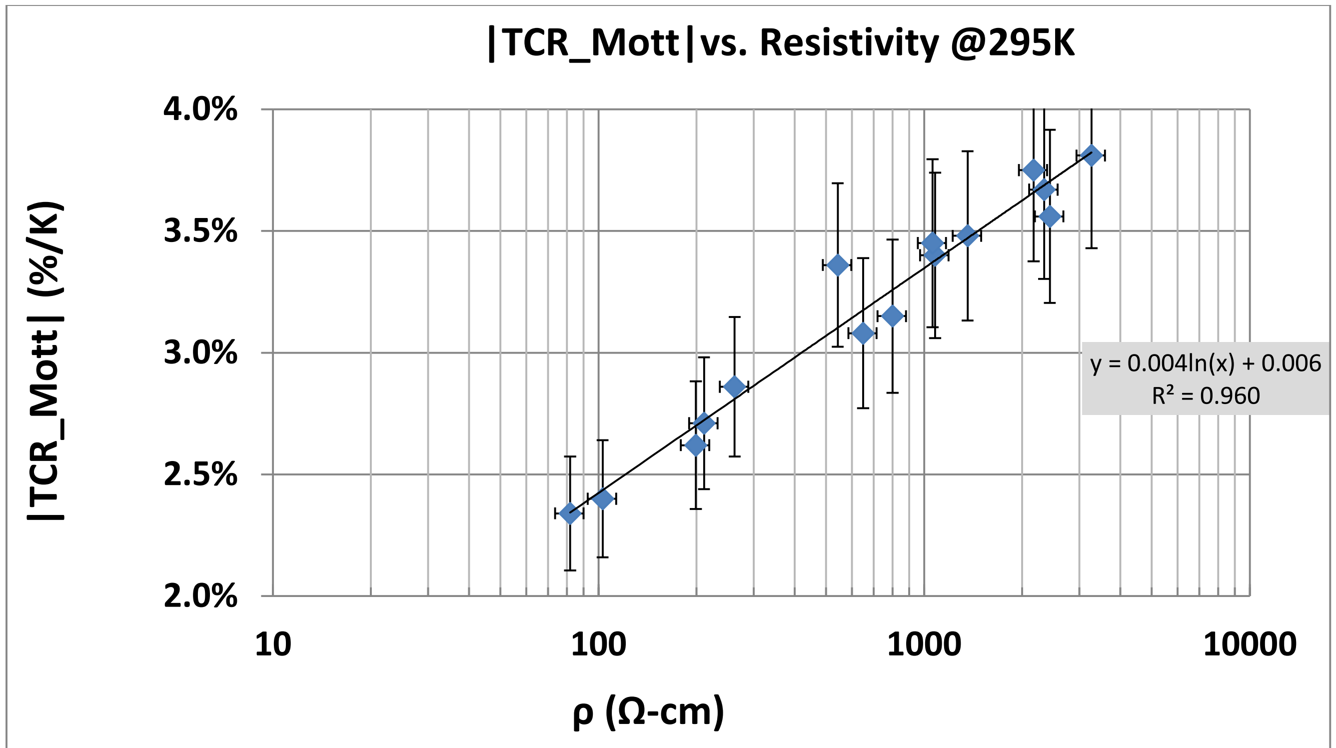

Figure 2-21. TCR_Mott vs. RT resistivity of various samples having different R_H and "r"
From this graph a comparison with the general equation of TCR, (Eq. 2-23) can be made.

Comparing y = 0.004ln(x) + 0.006 with the equation $TCR = \frac{p}{T}\ln\sigma_0 + \frac{p}{T}\ln\rho$, at room temperature there is a difference by a factor of five between the slope obtained from Figure 2-21 with the value of p/T.

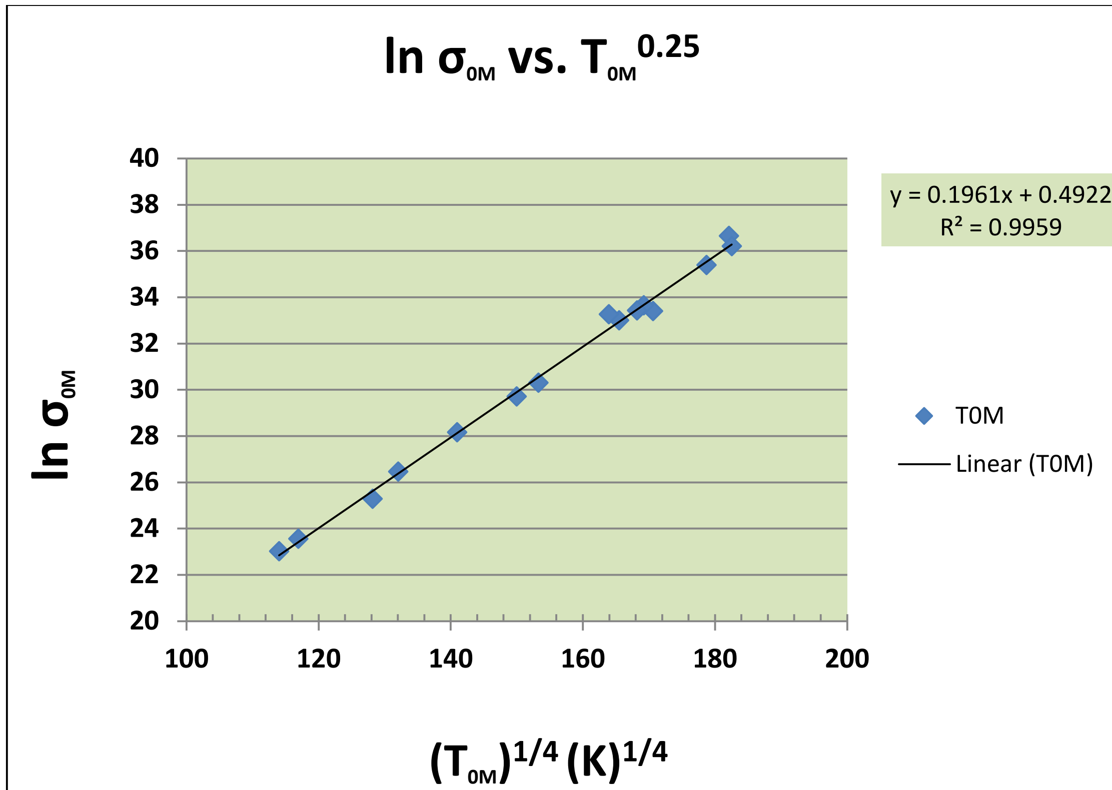

Figure 2-22. Ln σ_{0M} plotted against T_{0M}. The straight line represents the least- squares fit to the data.

The graph of $ln\ \sigma_{0M}\ vs.\ T_{0M}^{0.25}$ gives the equation by experimental data as,

$$ln\ \sigma_{0M} = 0.1961\ T_{0M}^{0.25} + 0.4922$$

Eq. 2-31

As the value σ_{0M} depend on the T_{0M}, the conductivity prefactor will not be a constant.
A correlation between conductivity prefactor and activation energy is known a Neyer-Neldel rule. In this case the relation can be written as,

$$\sigma_0 = \sigma_{00} e^{\left(\frac{T_0}{T_{MN}}\right)^p}$$

Here, T_{MN} is called the Meyer-Neldel temperature. Combining this equation with general conductivity Eq. 2-9 and using Eq. 2-18, TCR expression including Meyer-Neldel temperature can be derived as,

$$TCR = \frac{p}{T} * \frac{1}{1 - \left(\frac{T}{T_{MN}}\right)^{p}} \{\ln \rho + \ln \sigma_{00}\} \qquad \text{Eq. 2-32}$$

Then at room temperature T=295 K, and using the slope of the Figure 2-22 ,
$TCR = \frac{0.25}{295(1-0.1961*295^{0.25})} \{ln\, \rho + ln\sigma_{00})$= *0.0045* $\{ln\, \rho + ln\sigma_{00})$

The graph (Figure 2-21) of TCR vs. ρ gave the equation experimentally as;

$$TCR = 0.0042 ln\, \rho + 0.006$$

Hence the slope value 0.0042 is in close agreement with the value calculated by the modified equation Eq. 2-33. It can be seen for fixed “r” (for e.g., r=0.32) slopes are close to that shown in Figure 2-20. Recently, Dalvi et al[55] presented and alternate model to describe the conductivity of a variety of disordered materials using a hopping Meyer-Neldel rule. Thus, although the conductivity follows M-VRH behavior, the TCR reveals that the conductivity prefactor has a temperature dependence following a variable range hopping Meyer-Nedel rule.

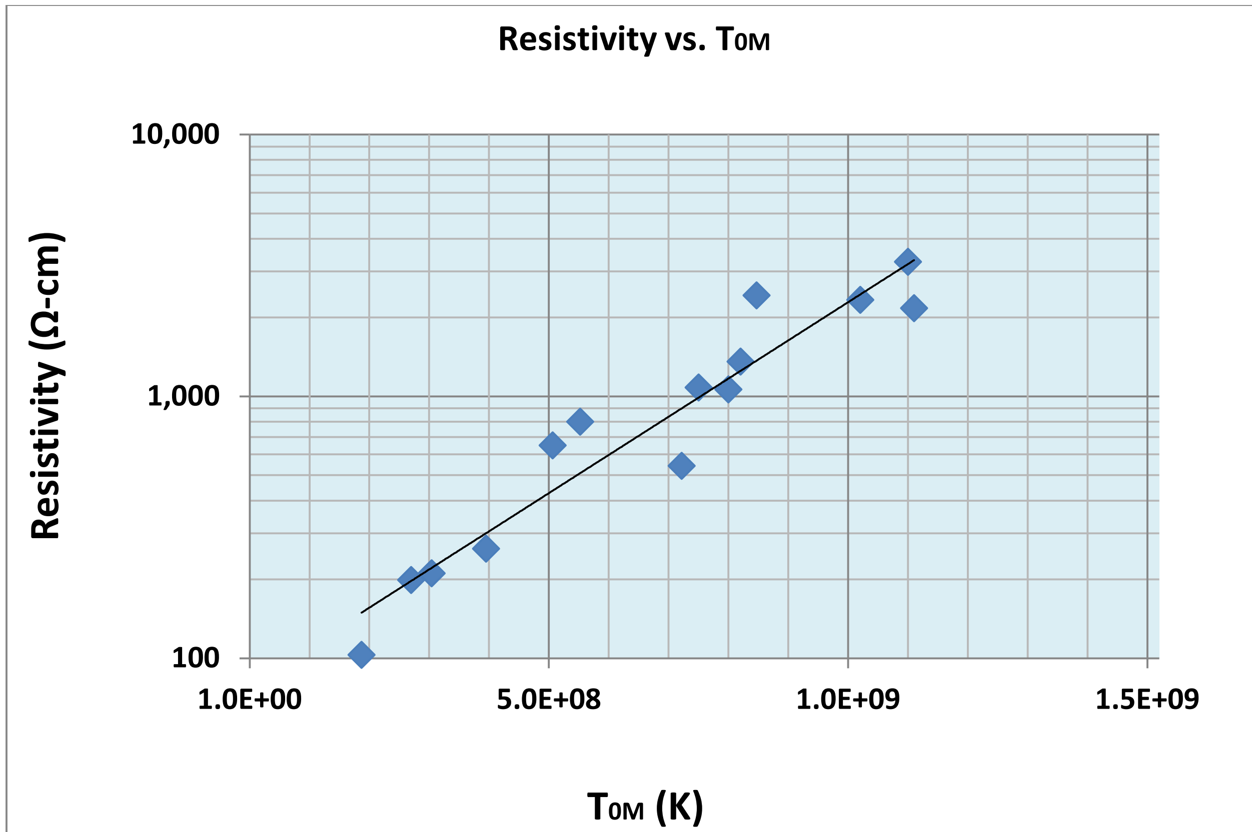

Figure 2-23. Resistivity vs. T_{0M} at RT of various samples showing an increasing trend of resistivity with the increase of Mott characteristic temperature

The Figure 2-23 shows, the RT resistivities vs. Mott characteristic temperatures for different samples varying in R_H at different boron dopings, which shows that there is a trend in increase of resistivity with the increase of the Mott characteristic temperature (an analogical term similar to activation energy). Further, it can be seen that as the T_{oM} increases both resistivity and TCR increase in similar manner. These values are presented in the Table 3.

Table 3. Sample properties - various parameters described in the text.

#	sccm	ID	"r"	R_H	Thick (Å)	Resistivity (Ω-cm)_by IV	TCR_Mott (%/K)	$\sigma_{0\text{-}M}$ 1/ (Ω-cm)	T_{0M} (K)
1	0.7	S140	0.12	60	523	3267	3.81	8.33×10^{15}	1.10×10^{9}
2	1	S063	0.17	55	1092	2433	3.5	3.23×10^{14}	8.47×10^{8}
3	1	S143	0.17	60	521	2336	3.68	2.37×10^{15}	1.02×10^{9}
4	1.9	S150	0.32	100	518	2170	3.75	5.3×10^{15}	1.11×10^{9}
5	1.9	S114	0.32	60	519	1360	3.48	4.10×10^{14}	8.20×10^{8}
6	1	S064	0.17	40	1060	1081	3.4	2.15×10^{14}	7.50×10^{8}
7	1.9	S103	0.32	49	2071	1062	3.45	3.30×10^{14}	8.00×10^{8}
8	1.9	S192	0.32	55	1060	800	3.15	1.45×10^{13}	5.52×10^{8}
9	1.9	S176	0.32	40	1071	650	3.08	7.99×10^{12}	5.06×10^{8}
10	1.9	MMG7-B	0.32	49	3270	543	3.1	2.80×10^{14}	7.22×10^{8}
11	1	270A	0.17	10	518	262	2.86	1.70×10^{12}	3.95×10^{8}
12	1.9	MMC2	0.32	16	3352	211	2.7	3.10×10^{11}	3.04×10^{8}
13	1.8	s30	0.3	16	505	199	2.62	9.60×10^{10}	2.70×10^{8}
14	1.9	MMC5	0.32	4	2778	103	2.4	1.71×10^{10}	1.87×10^{8}
15	1.8	2791	0.3	0.1	560	81.8	2.34	1.00×10^{10}	1.69×10^{8}

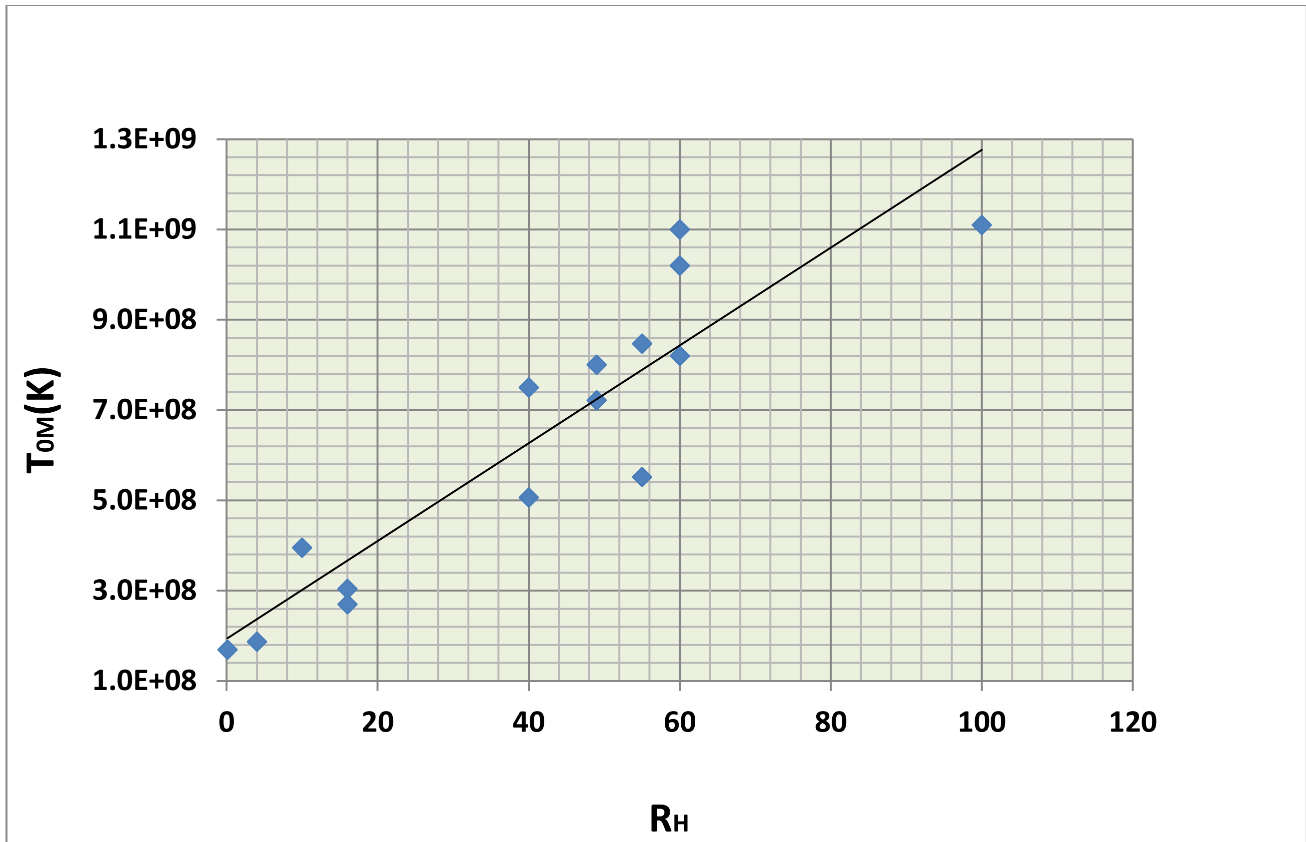

Figure 2-24. T_{0M} vs. R_H

The Mott characteristic temperature T_{0M}, shows almost a linear trend with the increase of R_H.

The increase of T_{0M} (this depends again on R_H) results in reduction of the conductivity, which is due to the increase of localization length (ξ). This increase is due to the reduction of numbers of traps as a result of better short range order in the a-Si:H matrix. Quantities that correlate with the Mott characteristic temperature are the localization length, hopping distance and energy. The localization length, R_{hop}, and hopping energy can be calculated by using the standard Mott expression. They are given by the wave function localization length,

$$\xi = \left(\frac{18}{\mathrm{K_B T_{oM}} N(\mathrm{E_F})}\right)^{1/3} \qquad \text{Eq. 2-33}$$

The hopping distance and hopping energy are, respectively,

$$R_{hop} = \frac{3}{8}(\frac{T_{0M}}{T})^{1/4} * \xi$$ Eq. 2-34

and, $$W_{hop} = \frac{1}{4}(kT)(\frac{T_{0M}}{T})^{1/4}$$ Eq. 2-35

The values obtained at 300K, assuming a density of state of 1x 10^{20} cm^{-3} eV^{-1} is presented in Table 4, which summarize the values obtained using Eq. 2-33 to Eq. 2-35 for the samples having four different R_H values at fixed boron doping ratio "r"= 0.32.

Table 4. Calculations of wave function localization length, hopping distance and energy at 300K for various R_H values using the Mott characteristic temperature assuming the density of state as indicated.

$N(E_f)$ [1 /cm^3 eV]	**Temp**	**R_H**	**T_{0M}(K)**	**loc length (ξ) (Å)**	***R_{hop}*(Å)**	***(W)$_{hop}$*, (meV)**	**at 300K, *R_{hop}/ξ***
1x10^{20}	300K	4	1.87x10^8	2.2	23.6	182	10.5
1x10^{20}	300K	16	3.04x10^8	1.9	22.6	205	11.9
1x10^{20}	300K	49	7.22x10^8	1.4	21.0	255	14.8
1x10^{20}	300K	100	1.11x10^9	1.2	20.3	284	16.4

The graphs in Figure 2-25 shows that with the increase of R_H, the T_{0M} increases and the localization length decreases. In chapter 3 this will be correlated with the structural configuration of these samples according to the amount of hydrogen. As the structural order improves, there will be less defects states (electrically-active defect states), resulting in an increase in the activation temperature and ultimately increases the resistivity and conductivity prefactors, as previously discussed.

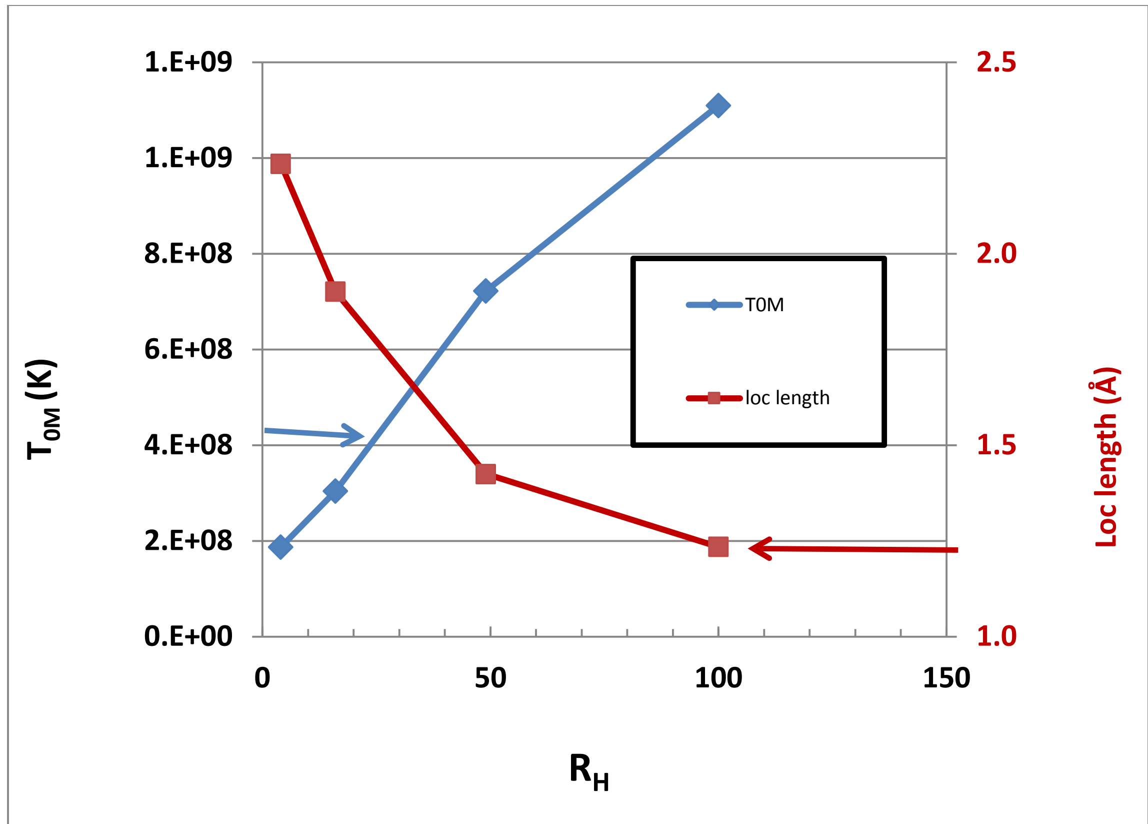

Figure 2-25. T_{oM} and localization length vs. R_H for the samples having fixed doping ratio "r"=0.32

The localization length, hopping distance and hopping energy (W_{hop}) at 300 K calculated are comparable with values reported by Khan[56] for amorphous silicon nanoparticles prepared by physical vapor condensation method. It is clear from the values presented in the Table 4 that, the hopping energy increases with the increase of the H-dilution and so does the value *"R_{hop}/ξ"*.

In the same way, the parameters obtained for various boron doping at fixed R_H (60) are presented in Table 5.

Table 5. Calculations of wave function localization length, hopping distance and energy at 300K for various boron doping using the Mott characteristic temperature

$N(E_f)$ [1 /cm^3 eV]	Temp	Boron doping "r"	T_{0M}(K)	loc length (ξ) (Å)	R $_{hop}$(Å)	$(W)_{hop}$ (meV)	at 300K, R_{hop}/ξ
$1x10^{20}$	300K	0.12	$1.10x10^9$	1.2	20.3	283	16.4
$1x10^{20}$	300K	0.17	$1.02x10^9$	1.3	20.4	278	16.1
$1x10^{20}$	300K	0.32	$8.20x10^8$	1.4	20.8	263	15.2

Figure 2-26 shows how the T_{0M} and localization length changes with the change in the boron doping for fixed R_H (60). Since there are more states available due to boron doping, the value of Mott characteristic temperature decreases, and the electrical conduction increases. Accordingly the localization length increases slightly.

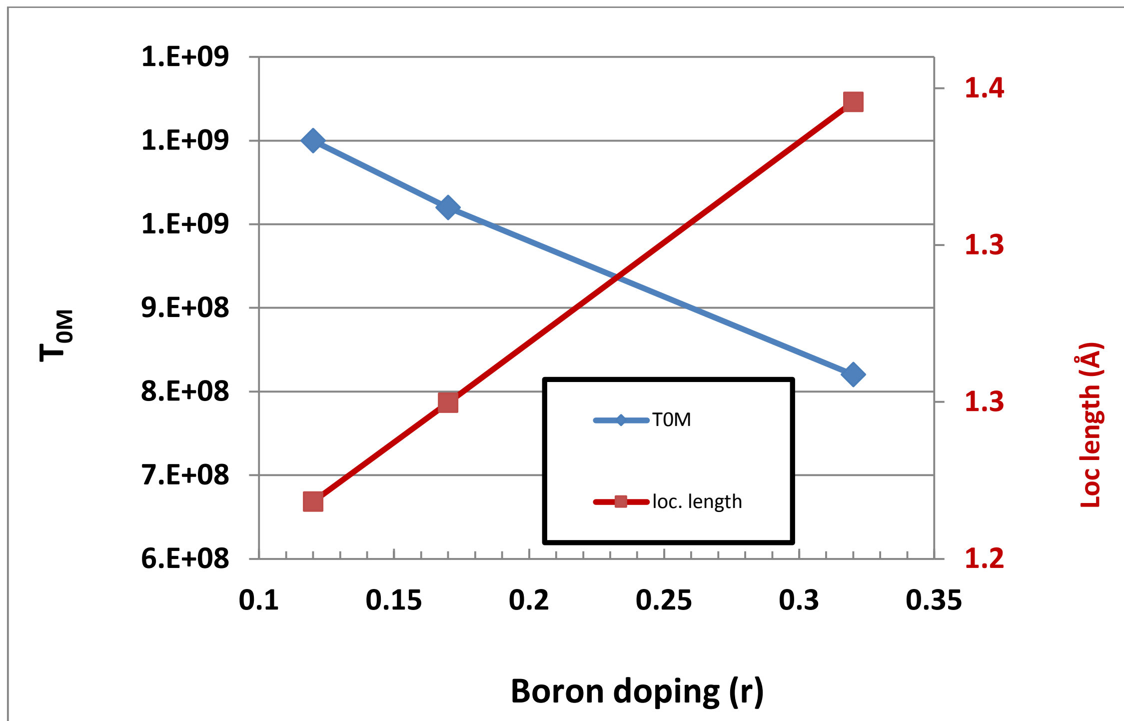

Figure 2-26. T_{oM} and localization length vs. boron doping for fixed R_H=60

Unlike in the case of R_H, in this case as the boron doping increases, the Mott parameter (T_{0M}) decreases, whereas the R_{hop} and localization length both increase only slightly. This may be an indication that the effect of hydrogen is strong compared to the boron incorporation. The hopping energy decrease with an increase of boron, as can be seen from the Table 5 and this is in the opposite direction to the R_H, as indicated by the Table 4. Hence, the structural re-arrangement in the a-Si:H matrix due to boron and hydrogen is playing the role in the electrical conduction due to localized states in these samples. This can be understood as a competition of boron and silicon to trap a hydrogen atom, as previously discussed. More about the structural changes will be elaborated on chapter 3.

The calculations of localization length, hopping distance and the hopping energy by using the T_{oM} value and a nominal value for DOS[57] of $N(E_F)$ ~$1x10^{20}$ $cm^{-3}eV^{-1}$ for the sample set having (a) fixed boron with different R_H, and (b) fixed R_H with different boron doping levels show that the conditions required for VRH are fulfilled. The conditions as described in the references by Yildiz[16], Khan[56]. The condition for hopping is given as,

$$W_{hop} \geq \mathrm{k\,T}$$

$$\text{sample thickness (d)} \gg R_{hop}$$

$$\frac{R_{hop}}{\xi} \geq 1$$

Therefore, it can be concluded that the conditions for the hopping are fulfilled, which indicate that the mechanism is VRH in the material system in the temperature range studied. Also the values obtained for the VRH parameters are close to those found in variety of

disordered systems. In addition, H Overhof[58] in his "Mott memorial lecture" reported that the T_{oM} values lie within the range of $1x10^8$ K to 1 $x10^9$ K and our values in all the samples are in this range. Therefore, the values obtained in this research for T_{oM} are in excellent agreement with the reported values by different authors. As discussed previously, this parameter is directly linked with the wave function localization length (ξ). Thus Table 4 shows that, with the increase of R_H, the ξ value decrease and hence decreases of R_{hop}. The wave function is more localized in the traps, making it difficult to hop to other traps, resulting in increase of resistance and hence the resistivity. Of course, this phenomenon depends on temperature, and can be seen an increase in R_{hop} with a decrease in temperature. The larger value of T_{0M} represents that larger energy is required (in the form of activation temperature,$T_{0M}^{0.25}$) to hop from one site to another for conduction, which make the material more highly resistive. A similar conclusion can be made for boron dependent samples in Table 5 in which the resistivity is less for higher boron doping, due to availability of substitutional sites for hopping due to doping.

2.6 Summary and Conclusion

The electrical conductivity and TCR studies show that, for most of the temperature range investigated, the temperature dependent conductivity is described by the Mott variable range hopping (VRH). The Mott conductivity prefactor (σ_{0M}) and characteristic temperature (T_{0M}) decrease with increasing boron doping for fixed H-dilution and increase with increasing dilution for fixed doping. The values of T_{0M} lie in the range of $1x10^8$ K to 1 $x10^9$ K which agrees well with literature.[58] For samples with low H-dilution, the conductivity is seen to deviate from Mott VRH and can be described by contributions from both Mott VRH and Efros-Shklovskii VRH. The total TCR is given by combination of both TCR_Mott and TCR_ES. In addition, a study of conductivity

prefactor with the Mott characteristic temperature leads to evidence of a “hopping” Meyer-Neldel rule recently discussed as a “universal” conduction model[55]. Finally the changes in the structural properties due to changes in hydrogen and boron in the a-Si:H matrix affect the electrical properties. This will be better quantified in chapter 3.

CHAPTER 3

OPTICAL CHARACTERIZATION

3.1 Raman Spectroscopy

When a monochromatic radiation of very narrow frequency band is scattered by matter, the scattered light not only consists of the radiation of incident frequency but also of frequencies above and below that of the incident light frequency. This process results from an inelastic collision of an incident photon and matter where, as a result of collision, the vibrational or rotational energy of the matter is changed by an amount ΔE. This form of scattering, in which the frequency of incident beam undergoes a definite change, was observed and studied by C.V. Raman in 1928 and is known as Raman Effect.

The scattering process under consideration involves the interaction of light with the vibrational modes of the material under investigation. Let E_i (=hν_i) and E_f (=hν_f) be initial energy of incident photon and final energy of the scattered photon with liberation of a phonon (or, several phonon modes). Also, let ω_1, ω_s and Ω_M be frequency of incident radiation, scattered and the difference between initial and final state respectively. If, as is the case for the measurements presented here, $E_f < E_i$, then $\omega_s = \omega_1 - \Omega_M$, where Ω_M is the frequency of the scattering phonon. In the Raman spectra several peaks can be observed, corresponding to the active phonon modes of the material under investigation[59, 29].

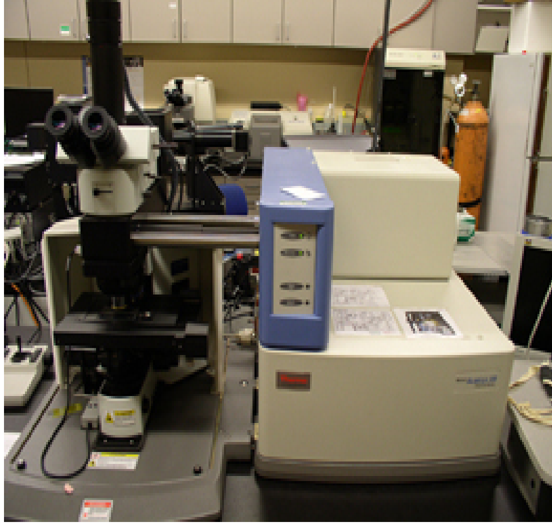

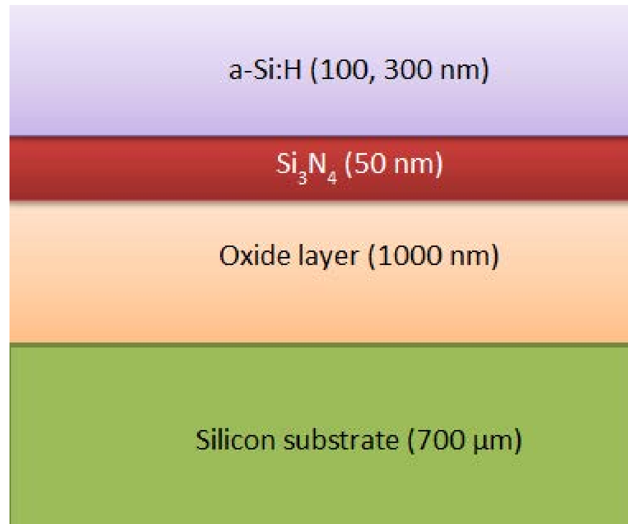

Figure 3-1. (a) Raman Spectrometer (UNT-CART) (b) Raman sample structure

Raman spectroscopy is one of the most widely used techniques to understand the local crystal structure of amorphous materials since it provides information about the bonding network order in such materials. It is a nondestructive measurement which provides information about the short range order (SRO) and mid-range order (MRO)[60,61,62]. The SRO of an amorphous material is usually associated with the nearest neighbor coordination[63] and the MRO involves the topology of the network at the level of third or fourth nearest neighbor and described by the size and distribution of rings of constituent atoms[33]. Various groups have used Raman spectroscopy to study the changes in the local crystal structure of a-Si:H by investigating the changes in the transverse optical (TO) and transverse acoustic (TA) modes of vibration[23,64,65,66]. These studies show that the intensity ratio of the TA and TO modes (I_{TA}/I_{TO}), full width half maximum of the TO mode (Γ_{TO}), and the central wavenumber (ω_{TO}) of the TO modes depend on growth method, growth temperature, and hydrogen content. In plasma enhanced chemical vapor deposition (PECVD) growth, the structural configuration of a-Si depends on the H-dilution of the silane precursor and the thickness of the thin film, and can

yield different states such as amorphous, nano/micro crystalline and polycrystalline phases[28,67]. In addition, structural changes in a-Si:H films due to hydrogen incorporation and doping have been reported[68,26,69,70]. The addition of boron results in local structural changes resulting from the formation of chemical bonds, such as B-Si and B-H-Si[69], results in an increase in bond angle and bond length, leading to a degradation of the SRO. Specifically, it has been shown that hydrogen diluted crystallization is mediated by insertion of H atoms into Si-Si bonds through the formation of a Si-H-Si bonding configuration when H atoms diffuse in a-Si:H matrix, resulting in improved crystallinity, i.e., improvement in SRO[70]. Infrared spectroscopic results[26,38] have shown that, with the addition of boron, there is a competition between boron and silicon to form bonds with the hydrogen, resulting in an increase in B-H stretching mode bonds and a decrease in Si-H bonds as the boron concentration is increased.

In preliminary work by our group[25], it was observed that an increase of Boron doping broadens Γ_{TO}, indicating retardation in the formation of microcrystals in the film, resulting in an increase in structural disorder. It was also shown that higher growth temperature and higher H-dilution promotes improvement in the atomic order of boron-doped a-Si:H films grown by PECVD.

In this work, room temperature Raman spectra from boron doped p-type a-Si:H thin films prepared by PECVD at two growth temperatures for various levels of H-dilution and boron doping will be presented, and the effect of these parameters on the phonon modes of vibration will be discussed. It is found that there is a strong relationship between the local structural order and the growth parameters of temperature, H-dilution and boron doping. The results show that, with either an increase of H-dilution or with increased growth temperature, the SRO

and MRO of the a-Si:H films improve, as evidenced by a decrease of both Γ_{TO} and the intensity ratio (I_{TA}/I_{TO}) of the TA and TO vibrational modes[22]. In addition, the effect of H-dilution on SRO and MRO decreases at increased sample growth temperature and, for samples with fixed H-dilution, an increase in boron doping results in a decrease in the SRO. Finally, the electrical resistivity of the samples prepared at the higher growth temperature correlates with Γ_{TO} and ω_{TO}, where the resistivity increases with decreasing $\Gamma_{TO,}$ and increasing ω_{TO} results from the improvement in SRO.

3.2 Experimental

Several a-Si:H thin films were grown by PECVD at the substrate temperatures of 275 °C and 365 °C. The thickness of the films investigated ranged from approximately 1000 Å to 3000 Å. The flow rate ratio of boron to silane, defined as "r" = $[BCl_3]/[SiH_4]$, and H-dilution to silane ratio "R_H"=$[H_2]/[SiH_4]$, were varied to produce films with differing hydrogen and boron concentrations. The samples reported here were grown at R_H values ranging from 4 to 55 and with "r" values of 0.17 and 0.32. A Thermo Electron Almega XR Raman Spectrometer with a 532 nm laser as an excitation source and a 2.5 micron spot size was used to obtain room temperature Raman spectra.

3.3 Results and Discussion

The Raman spectra for different growth temperatures and H-dilutions for a fixed flow rate ratio of boron r = 0.32 are shown in the Figure 0-2. In agreement with the growth phase diagram[28], increasing H-dilution for a fixed boron doping and growth temperature results in a decrease in Γ_{TO}, indicating better structural order with an increase of H-dilution. Specifically, Figure 3-2(a) shows spectra obtained for a fixed H-dilution of R_H = 16 for films grown at 275 °C

and 365 °C. It is clearly seen that when either R_H, growth temperature, or both increase, Γ_{TO} narrows, indicating an improvement in SRO. In addition, the intensity ratio, I_{TA}/I_{TO}, decreases, indicating an improvement in the MRO. The spectra shown in Figure 3-2(b) better illustrate the effects of H-dilution on the improvement in local structural order. At the lower growth temperature, an increase in hydrogen concentration results in a substantial improvement in the local structure (i.e., SRO and MRO), as evidenced by a decrease of both Γ_{TO} and the intensity ratio (I_{TA}/I_{TO}) of the TA and TO vibrational modes. This improvement in local order is further supported by the spectra shown in the inset, which shows that, at higher H-dilutions, the TO peak shifts to higher wavenumber.

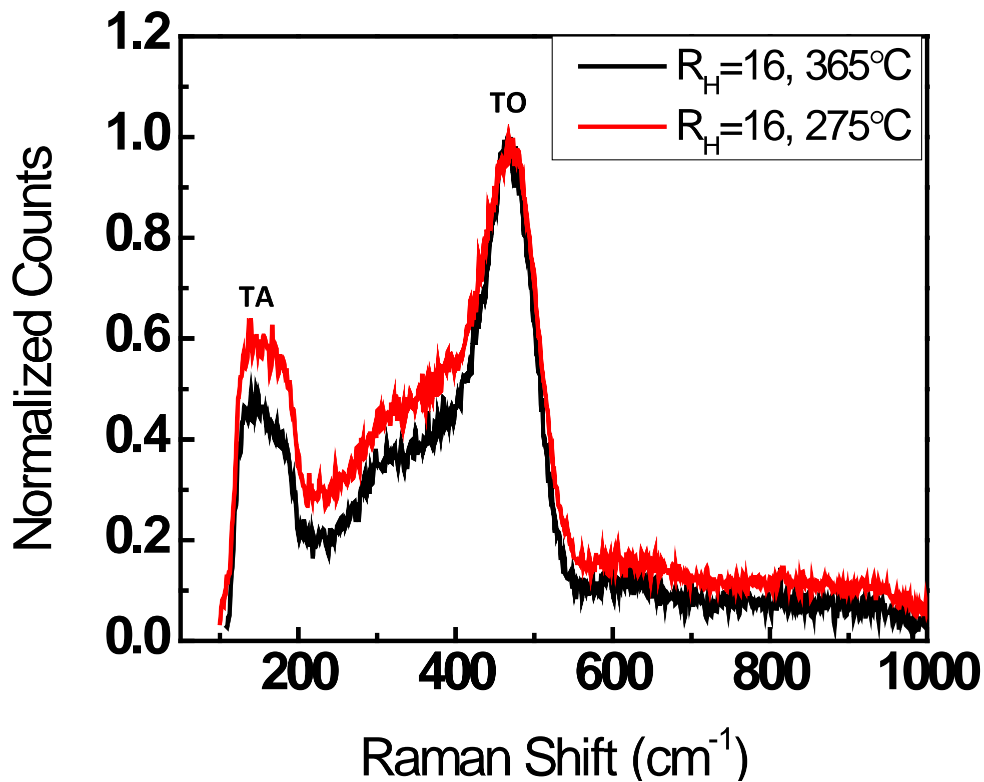

(a)

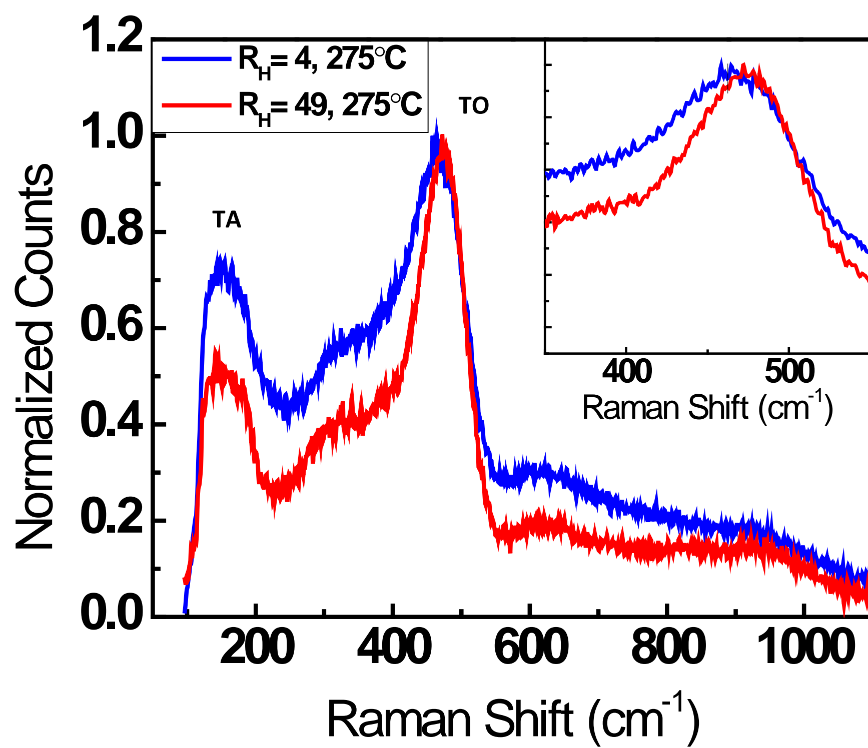

(b)

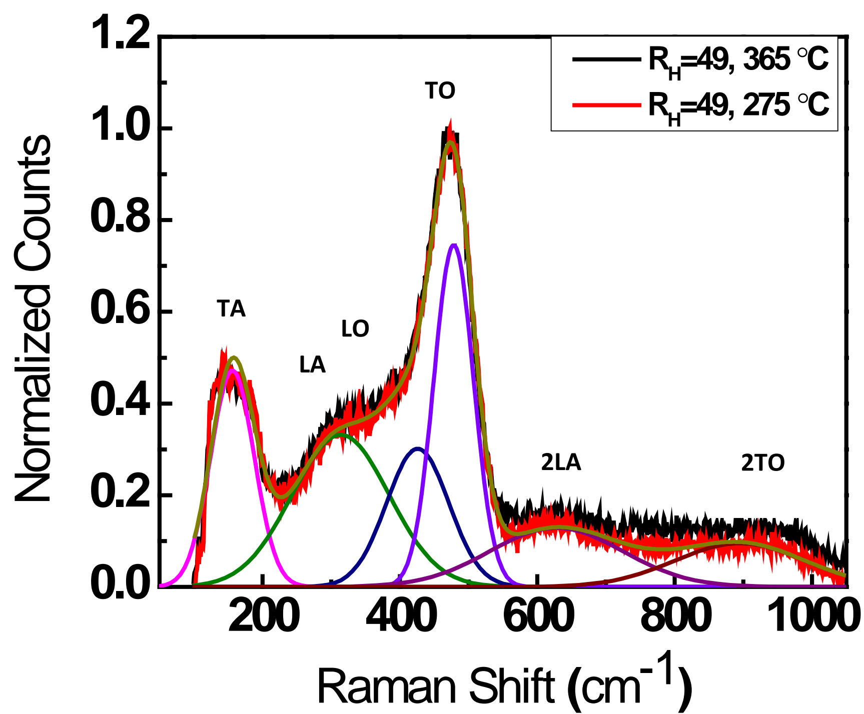

(c)

Figure 3-2. Representative Raman spectra for the doping level r = 0.32 (a) for a fixed H-dilution at growth temperatures 275 °C and 365 °C (b) for the H-dilutions of $R_H = 4$ and 49 at a growth temperature of 275 °C and (c) For the H-dilution ($R_H = 49$) at growth temperatures 275 °C and 365 °C, showing deconvoluted Raman peaks from left to right: TA (ω=155.5cm^{-1}), LA (ω=312.1 cm^{-1}), LO (ω=425.5 cm^{-1}), TO(ω=477.8 cm^{-1}), 2LA (ω=625.6 cm^{-1}), tentative 2TO (ω=895.8 cm^{-1}).

Figure 3-2© illustrates effect of growth temperature on the ability of hydrogen to improve the short- and mid-range order of the a-Si:H thin film. This figure shows spectra obtained for the highest H-dilution of $R_H = 49$ for films grown at 275 °C and 365 °C. At this high H-dilution the Raman spectra obtained at both growth temperatures are virtually identical. This can be understood in terms of changes in the amorphous structure due to bonding nature of silicon with hydrogen. Higher H-dilution affects the growth structure as the kinetics of atom incorporation changes by changing the constituent elements by the formation of either Si-H or $Si\text{-}H_2$. It has been shown by *ab initio* calculations that mobile hydrogen atoms break strained silicon bonds to form Si-H and $Si\text{-}H_2$[35]. From the infrared spectroscopy it has been reported that, with the increase of H-dilution, silicon monohydride absorption peaks increase in strength whereas silicon dihydride absorption peaks decrease[26]. For fixed doping and dilution, the silicon monohydride absorption peak is significantly larger for lower growth temperature,[71] which can be attributed to additional hydrogen atoms being absorbed. On the other hand, the higher growth temperature adds surface mobility to the absorbed reactant species, which increases the likelihood of lower energy bond configurations. Further, the higher growth temperature increases the desorption or dissociation of weakly bonded species, reducing the net deposition

rate and increasing the likelihood that stronger bond configurations are prevalent. Thus, the improvement in SRO and MRO at each growth temperature due to the formation of Si-H and $Si-H_2$ bonds overcomes any action of the higher growth temperature to decrease the absorption of hydrogen. It has been shown in glow discharge grown undoped a-Si:H that mechanical stress is not primary factor for the change of central frequency position of the TO mode[72]. As a result, it is concluded that the improvement in the local order results primarily from the increase in H-dilution.

As previously discussed, growth temperature and H-dilution causes significant changes in the structural order of a-Si:H thin films. To better quantify the observations shown in Figure 0-2©, Gaussian deconvolution was performed on each spectrum, using 6 Gaussian peaks representing the TA, LA, LO, TO phonon modes and replica peaks of the LA and TO phonon modes, respectively. The results are shown in Figure 0-3. Table 6 shows the Raman parameters measured for various samples.

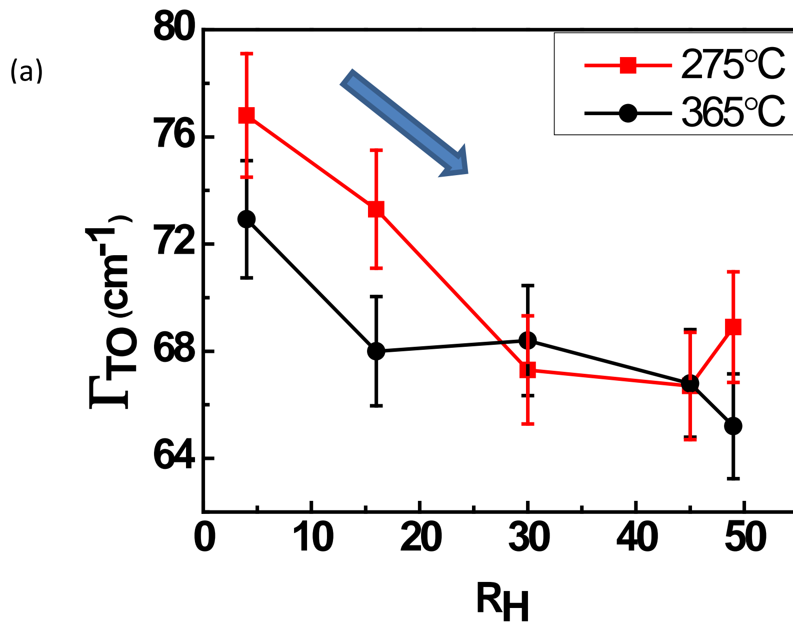

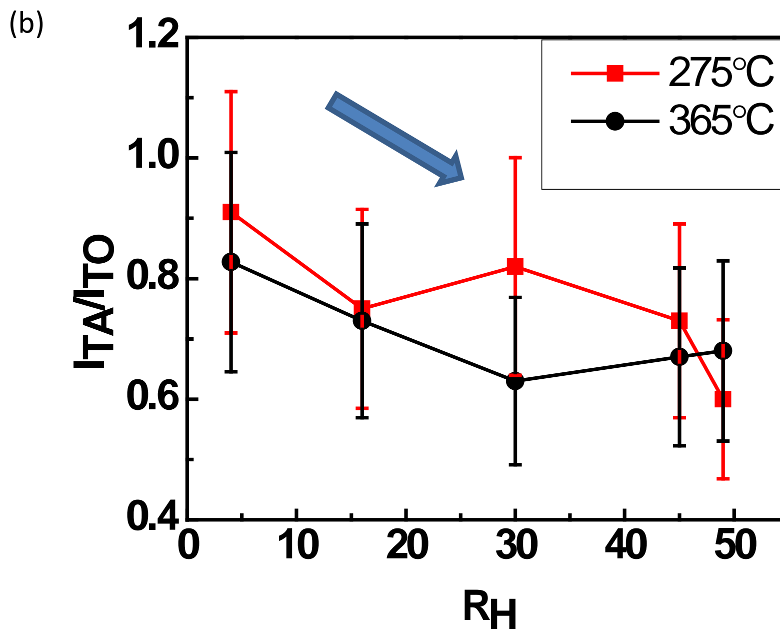

Figure 3-3. (a) Γ_{TO} vs. H-dilution, indicating improvement in SRO with increase of H-dilution for "r"=0.32 (b) intensity ratio (I_{TA}/I_{TO}) vs. H-dilution indicating improvement in MRO with increase of H-dilution for "r"=0.32,

Figure 3-3(a) shows Γ_{TO} plotted with respect to the H-dilution ratio (R_H) for both growth temperatures. As the H-dilution is increased, Γ_{TO} decreases, indicating improvement in the SRO. It can be seen from Figure 3-3(a) that, the effect of growth temperature on structural order decreases with increasing H-dilution. Figure 3-3(b) shows a gradual decrease in the intensity ratio I_{TA}/I_{TO} with an increase of H-dilution, indicating a trend of gradual improvement in the MRO. It can be speculated that the topology of the network improves with the increase of H-dilution[33].

Figure 3-4 shows the influence of boron doping on the SRO, illustrated for two H-dilutions (R_H =40 and 55) and two different boron doping levels (r = 0.17 and 0.32)

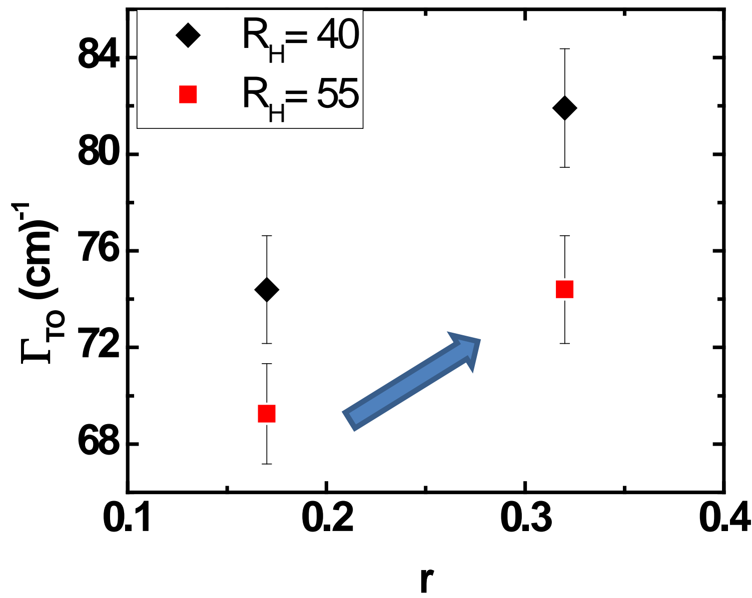

(a)

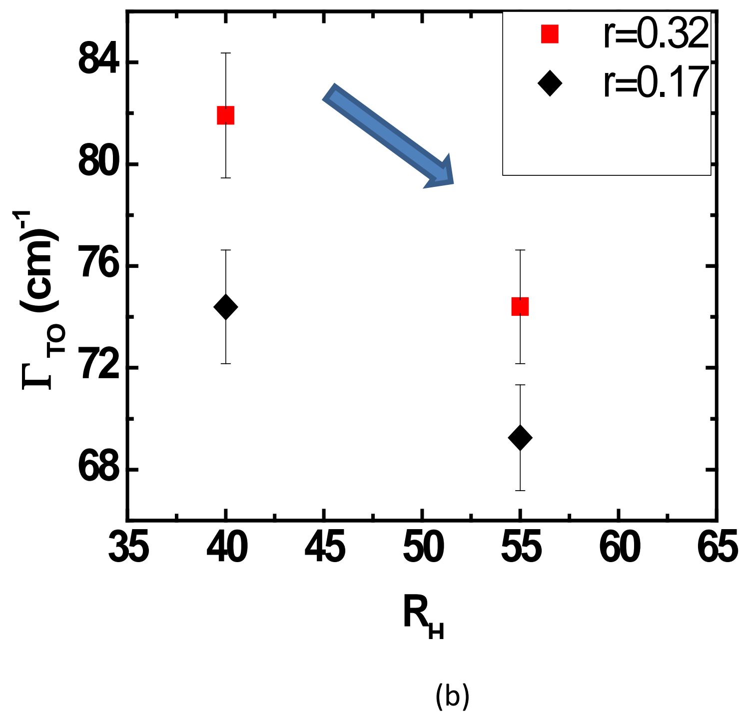

(b)

Figure 3-4. (a) Γ_{TO} vs. boron incorporation, “r”, and (b) Γ_{TO} vs. H-dilution, R_H.

As is seen in Figure 3-4(a) for both H-dilutions shown, Γ_{TO} increases with increasing boron concentration, indicating degradation in SRO. Illustrated differently, as shown in Figure 3-4(b), Γ_{TO} decreases with increasing H-dilution for each boron concentration, indicating that an increase in hydrogen concentration overcomes the effects of boron on the SRO. This suggests that there is a competition between boron and silicon to capture a hydrogen atom and that the degradation in SRO results from a rearrangement of chemical bonding in a-Si:H.

Table 6. Raman parameters (TO frequency, TO line width and intensity ratio I_{TA}/I_{TO}) for measured a-Si:H thin film samples.

Growth Temperature (°C)	Thickness (Å)	Boron doping $[BCl_3]/[SiH_4]$	H-dilution $[H_2]/[SiH_4]$	ω_{TO} (cm)$^{-1}$	Γ_{TO} (cm)$^{-1}$	I_{TA}/I_{TO}
365	2778	0.32	4	473.1±1.9	72.9±2.6	0.83±0.17
365	3199	0.32	16	474.1±1.9	68±2.4	0.73±0.15
365	3199	0.32	30	477.5±1.9	68.4±2.4	0.63±0.13
365	3162	0.32	45	475.2±1.9	66.8±2.3	0.67±0.13
365	2986	0.32	49	477.2±1.9	65.2±2.3	0.68±0.14
275	3000	0.32	4	473.8±1.9	76.8±2.7	0.91±0.18
275	3000	0.32	16	473.8±1.9	73.3±2.6	0.75±0.15
275	3000	0.32	30	477.0±1.9	67.3±2.4	0.82±0.16
275	3000	0.32	45	475.3±1.9	66.7±2.3	0.73±0.15
275	3000	0.32	49	477.8±1.9	68.9±2.4	0.6±0.12
365	1060	0.32	55	472.0±1.7	74.4±2.2	0.34±0.02
365	1071	0.32	40	471.9±1.7	81.9±2.5	0.44±0.03
365	1092	0.17	55	479.0±1.7	69.3±2.1	0.52±0.04
365	1060	0.17	40	476.5±1.7	74.4±2.2	0.48±0.03

The Raman results show that the structural properties depend strongly on growth temperature and the plasma chemistry. It is well known that hydrogen passivates the dangling bonds of a-Si[33]. However as seen from Figure 0-2© and Figure 0-3(a), increasing the hydrogen supply in the plasma at the higher growth temperature has little effect on the Raman spectra. This indicates that the growth kinetics of PECVD a-Si:H favor hydrogen incorporation into the a-Si thin film at lower growth temperatures. The results presented here agree with and extend those obtained at lower temperatures[73] which showed that the development of the local

structure (SRO and MRO) in a-Si:H depends on the initial ordering of the amorphous network which, in turn, is determined by the growth temperature.

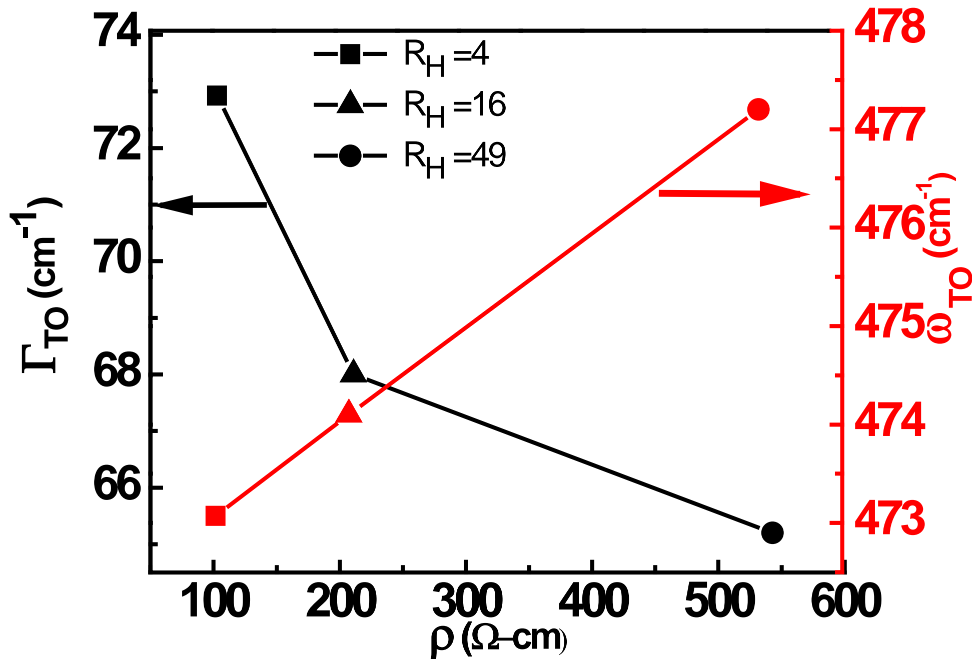

Figure 3-5. Line width and central frequency of TO mode vs. RT resistivity for "r" = 0.32, showing improvement in SRO and higher resistivity for higher H-dilution at 365 °C

Figure 3-5 shows a correlation of electrical resistivity with Γ_{TO} and ω_{TO}. In Figure 3-5, Γ_{TO} and ω_{TO} are plotted with respect to resistivity for various H-dilutions from 4 to 49 for samples with fixed boron doping (r = 0.32) and growth temperature (365 °C). The decrease in the linewidth and shift to higher wavenumber of the TO peak with increasing H-dilution indicate that there is a continuous improvement in the structure of the amorphous network on the short range scale. Thus, the increase in resistivity can be understood as a result of the improvement in the local order of the a-Si:H thin film. Similar results in fluorinated a-Si:H prepared by the glow discharge deposition method was reported by relating the central frequency of TO mode with the dark

conductivity[74]. It will be interesting to determine if this applies to growth conditions other than H-dilution.

3.4 Summary and Conclusion

The effects of H-dilution and boron doping on the structural properties of amorphous silicon thin films prepared by plasma enhanced chemical vapor deposition are reported and discussed. The results of Raman measurements obtained from a variety of samples of differing hydrogen and boron concentrations grown at two temperatures show that the short- and mid-range order improves with either an increase of H-dilution or higher growth temperature. The effect of growth temperature on the ability of hydrogen to improve the short- and mid-range order decreases as the growth temperature is increased. This is attributed to dissociation of weakly bonded species at higher growth temperature, leading to less hydrogen absorption. For fixed H-dilution, an increase in boron doping results in a decrease in the short-range order, indicating that boron rearranges the a-Si:H matrix either by the appearance of B-H bonds, or Si-H or B-H-Si complex. Finally, a direct correlation is seen between the electrical resistivity and the short-range order for samples of differing H-dilution grown at the higher growth temperatures.

The competition to capture hydrogen by silicon and boron by MIR-IR data[26] agrees with the Raman results as explained. Finally, a direct correlation is seen between the electrical resistivity and the short-range order for samples of differing H-dilution grown at the higher growth temperatures. Such a correlation, if sufficiently quantified, could lead to the use of purely optical measurements to determine the electrical conduction properties of a material.

CHAPTER 4

SUMMARY/ CONCLUSION/ FUTURE DIRECTIONS

The objective of the research was to understand the electrical conduction mechanism in the amorphous silicon thin films, which were prepared at different growth conditions. Variation of boron doping and H-dilution was used with different thicknesses of the samples, which are prepared by PECVD method. It was found that the film resistivity increases with the increase of H-dilution and decreases with the increase of the boron doping. The increase of hydrogen increases the mobility gap, which increases the resistivity of the materials, and TCR. It is shown that, TCR increases with the increase of resistivity and resistivity is the quantity affected with the combination of doping and dilution.

In almost all samples, it was observed that the electrical conduction mechanism is dominated by the Mott variable hopping mechanism. However, at lower temperatures there is evidence of an Efros Skhlovskii-variable range hoping in addition to the M-VRH. That the conductivity mechanism deviates from M-VRH to ES-VRH is due to the appearance of a Coulomb gap in the vicinity of the Fermi level. In such a case, the total conductivity is described by the sum of M-VRH and ES-VRH contributions, and this combination also described well the TCR results.

From the electrical results, it was found that, with the increase of H-dilution, the Mott characteristic temperature (T_{0M}) increases and hence the TCR increases. The Mott conductivity prefactors also are found to increase with the increase of H-dilution or decrease of boron doping. The localization wave function, hopping distances and hopping energies were also calculated and shown to be in agreement with the VRH mechanism. The characteristic

temperature calculated lies between $1x10^8$ K to $1x10^9$ K, which agrees with the literature for most of the amorphous silicon materials prepared by different growth methods.

The results presented here show that the electrical properties are strongly influenced by the structural changes in the materials due to the addition of boron and hydrogen and the growth conditions.

To better correlate the structural and electrical properties, Raman spectroscopy was used to obtain the structural changes resulting from the addition of boron, hydrogen and/or growth conditions. This was accomplished through the study of the transverse optical (TO) and transverse acoustic (TA) Raman modes to relate changes in short- and mid- range order to the effects of boron and hydrogen incorporation. The Raman results show that with an increase of hydrogen and/or growth temperature, both short and mid-range order improve, whereas the addition of boron always results in the degradation of short range order due to the formation of different boron/Si complexes. These results correlated well with the measured values of resistivity.

The increase of H-dilution affects the bonding nature of hydrogen in the a-Si:H matrix and Si-H bonding is the main cause for the structural improvement in the samples rather than Si-H_2 . Infrared spectroscopy measurements[26] have recently revealed a counter dependence of the B-H and the Si-H chemical bond on the boron dopant supply and on the H-dilution, resulting in a competition between boron and silicon to capture a hydrogen atom. Raman spectra also show the inverse effect between boron doping and hydrogen dilution in a-Si:H samples in agreement with electrical conductivity data.

A continuation of these studies can be a future direction for upcoming researchers in similar fields. Nano-composite materials may be developed by addition of nano dots, wires, or rods into the amorphous silicon matrix there by creating heterostructure materials with adjustable hopping conduction leading to improvement in IR detection based on bolometric detection. Connecting the conduction mechanism with their influence on electrical noise would also be an interesting future direction. For devices like IR detectors in which TCR and noise are important quantities, such composite materials may be tailored to reduce noise and enhance TCR. Such results would have impact on many applications other than IR detectors, such as solar cells, thin film transistors, and photon detectors as sensors.

APPENDIX

X-RAY PHOTOELECTRON SPECTRA (XPS) of REPRESENTATIVE AMORPHOUS SILICON THIN FILM

X-ray photoelectron spectroscopy (XPS) was used to identify the chemical species contained in the sample. A bi-layer (*a-Si/SiN (bi-layer: a-Si/siN/Si)* sample's XPS spectra is shown as an example.

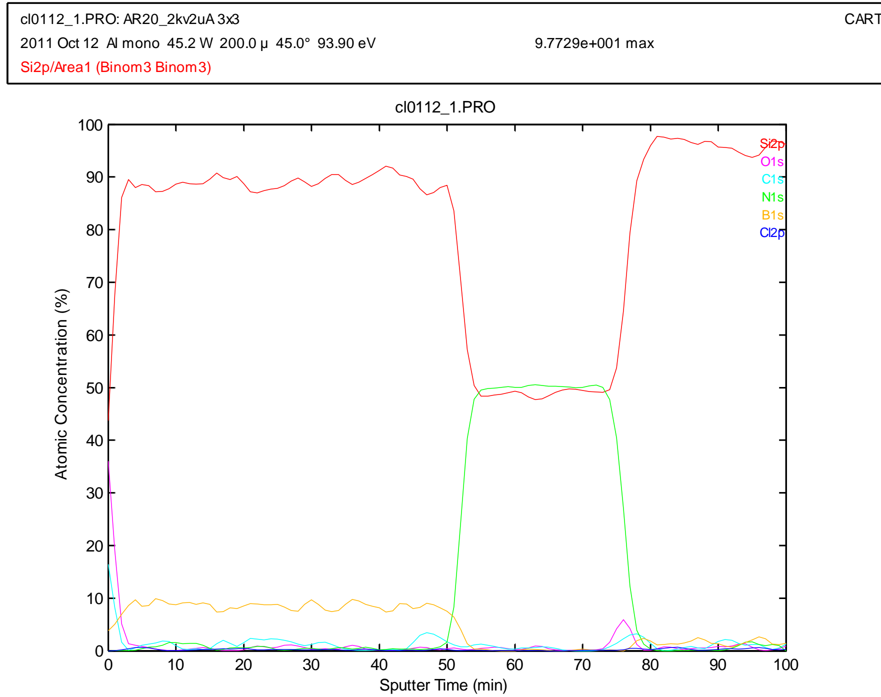

Figure . XPS spectra for bilayer of a-Si/SiN (bi-layer: a-Si/siN/Si) on silicon. The etch rate is 40 Å/ minute.

The spectra shows about 10 % of boron in the a-Si layer and nearly stoichiometric of silicon and nitrogen in the SiN layer. The calculation shows that the boron concentration is about 1.3×10^{22} cm^{-3}. Not all these boron atoms participated in conduction.

REFERENCES

[1] Ed. R.A. Street, in "Technology and Applications of Amorphous Silicon", Springer Series (2000)

[2] T Schimert, C. Hanson, J. Brady, T. Fagam, M Taylor, S B Cardel, R. Gooch, M.Gohlke, and A.J. Syllaios, " Advances in small-pixel, large-format, Si bolometer arrays", Proc. SPIE, Vol. 7298, 72980T, (2009)

[3] http://www.sofradir.com

[4] www.ulis-ir.com

[5] N.F. Mott and E.A. Davis, " electronic process in Non-Crystalline Solids", Clarendon, Oxford, (1979)

[6] Adam Lewis," Evidence for the Mott Model of Hopping Conduction in the Anneal Stable State of Amorphous Silicon", Phys. Rev. Lett. Vol. 29, (1972)

[7] J. H. Castilho, I. Chambouleyron, F. C. Marques, C. Rettori, and F. Alvarez "Electrical conductivity of amorphous silicon doped with rare-earth elements", Phys. Rev. B Vol. 43, 11, (1991)

[8] S. K. Ajmera, A.J. Syllaios, Gregory S. Tybera, Michael F. Taylora, and Russell E. Hollingsworth, "Amorphous Silicon Thin-Films for Uncooled Infrared Microbolometer Sensors", Proc. of SPIE Vol. 7660, 766012-1 to 766012-8.

[9] Ralph Rosenbaum "Crossover from Mott to Efros-Shklovskii variable-range-hopping conductivity in In_xO_y films", Phy. Rev. B, Vol. 44, Num. 8, (1991)

[10] R. Abdia, A. El Kaaouachi , A. Nafidi, G. Biskupski , J. Hemine" Variable range hopping conductivity and negative magnetoresistance in n-type InP semiconductor", Solid state electronics 53, (2009)

[11] Moon Sung Kang, Ayaskanta Sahu, David J. Norris, and C. Daniel Frisbie “Size- and Temperature-Dependent Charge Transport in PbSe Nanocrystal Thin Films”, pubs.acs.org/NanoLett

[12] Abdelfattah Narjis, Abdelhamid El Kaaouachi, Abdelghani Sybous, Lhoussine Limouny, Said Dlimi, Abdessadek Aboudihab, Jamal Hemine, Rachid Abdia, Gerard Biskupski “ Variable Range Hopping in Hydrogenated Amorphous Silicon-Nickel Alloys”, Journal of Modern Physics, 3, 517-520, (2012)

[13] Tulay Serin, Abdullah Yildiz, Necmi Serin, Nurcan Yildirim, Figen Ozyurt, And Mehmet Kasap, “Electron–Electron Interactions in Sb-Doped SnO2 Thin Films” Journal of Electronic Materials, Vol. 39, No. 8, (2010)

[14] A. Yildiz and M. Kasap”Variable-Range Hopping Conductivity in InGaN”, CP899, Sixth International Conference of the Balkan Physical Union, edited by S. A. Cetin and I. Hikmet© 2007 American Institute of Physics

[15] N. Aoki, K. Nara, and Y. Ochiai “Coulomb Gap Energy in Amorphous SixGe1-x Films”, phys. stat. sol. (b) 218, 5 (2000)

[16] Abdullah Yildiz, Necmi Serin, Tulay Serin, and Mehmet Kasap “Crossover from Nearest-Neighbor Hopping Conduction to Efros–Shklovskii Variable-Range Hopping Conduction in Hydrogenated Amorphous Silicon Films”, Japanese Journal of Applied Physics, Vol. 48 (2009)

[17] Crupi, S. Mirabella, D. D’Angelo, S. Gibilisco, A. Grasso, S. Di Marco, F. Simone, and A. Terrasi, “Anomalous and normal Hall effect in hydrogenated amorphous Si prepared by plasma enhanced chemical vapor deposition”, Journal of Applied Physics, Vol. 107, (2010)

[18] N. Savvides "Effects of hydrogenation and doping on the conductivity and density of defect states in amorphous silicon", J. Appl. Phys. 56 (10), 15 Nov. (1984)

[19] W Wei , Gangyi Xu, Jinliang Wang, Tianmin Wang "Raman spectra of intrinsic and doped hydrogenate nanocrystalline silicon films", Vacuum 81, (2007)

[20] N M Liao, W Li, Y D Jiang, ZM Wu, S B Li, Z Liu, Z Li, X Jin and Y X Chen "Electron irradiation effects on the properties of heavily phosphorus-doped a-Si :H films prepared from undiluted silane", J. Phys. D: Appl. Phys., Vol. 41, (2008)

[21] Maley, N. and Lannin, J. S., "Influence of hydrogen on vibrational and optical properties of a-$Si_{1-x}H_x$alloys", Phy. Rev.B **36** (1987)

[22] P Danesh, B Pantchev, K Antonova, E Liarokapis, B Schmid, D Grambole and J Baran, "Hydrogen bonding and structural order in hydrogenated amorphous silicon prepared with hydrogen-diluted silane", J. Phys. D: Appl. Phys., Vol. 37, (2004)

[23] Marinov and Zotov, "Model investigation of the Raman spectra of amorphous silicon", Phys. Rev. B 55, 2938, 1997

[24] Zhi Li, Wei Li, Yadong Jiang, Haihong Cai, Yuguang Gong and Jian He " Raman characterization of the structural evolution in amorphous and partially nanocrystalline hydrogenated silicon thin films prepared by PECVD", J. Raman Spectrosc., 42, 415–421,(2011), DOI 10.1002/jrs.2711

[25] A. J. Syllaios, S. K. Ajmer, G. S. Tiber, C. Littler, R. E. Hollingsworth "Raman Characterization of Protocrystalline Silicon Films", Mater. Res. Soc. Symp. Proc. Vol. 1153, 2009

[26] N. Ross, K. Shrestha, O. Chyan, C. L Littler, V. C. Lopes, and A. J. Syllaios, "Spectroscopic Study of the Chemical Bonding Structure in Amorphous Silicon Thin Films", MRS Proceedings, Vol. 1536/2013, DOI: http://dx.doi.org/10.1557/opl.2013.752

[27] Schropp and Zeman "Amorphous and microcrystalline silicon solar cells", Kluwer Academic Publishers

[28] R.W. Collins, A.S. Ferlauto, G.M. Ferreira, J. Koh, C. Chen, R.J. Koval, J.M. Pearce, C.R. Wronski, M.M. Al-Jassim, and K.M. Jones, "Application of deposition phase diagrams for the optimization of a-Si:H based materials and solar cells", Mat. Res. Soc. Symp. Proc. Vol. **762**, A10.1.1 (2003).

[29] C. Kittel, "Introduction to Solid State Physics", John Wiley and Sons Inc.

[30] M. Stutzmann; "Data on hydrogen in a-Si:H from diffusion and effusion studies", Feb 1998; Properties of Amorphous Silicon and its Alloy, Ed. TIM SEARLE, University of Sheffield, UK

[31] D.B. Saint John, H.B. Shin, M.-Y. Lee, S. K. Ajmera, A.J. Syllaios, E.C. Dickey, T.N. Jackson, and N.J. Podraza, "Influence of microstructure and composition on hydrogenated silicon thin film properties for uncooled microbolometer applications", J. of App. Phys 110, 033714 (2011)

[32] J.I. Pankove and D.E. Carlson; "Electrical and Optical Properties of Hydrogenated Amorphous silicon", Ann. Rev. Mater. Sci, (1980)

[33] R.A. Street, "Hydrogenated amorphous silicon", Cambridge University Press

[34] Xunming Deng and Eric A. Schiff "Amorphous Silicon–based Solar Cells"

[35] S. Chakraborty and D.A. Drabold; "Static and dynamic properties of hydrogenated amorphous silicon with voids", Phy Rev B **79**, 115214, (2009)

[36] Spear and LeComber; " Electronic properties of substitutionally doped amorphous Si and Ge", Philos. Mag., B33:935, (1976)

[37] C. C. Tsai; “Characterization of amorphous semiconducting silicon-boron alloys prepared by plasma decomposition”, Phy. Rev. B, Vol. **19**, Feb. (1979)

[38] S. C. Chen and M. Cardona; “Infrared and far-infrared absorption of B- and P-doped amorphous Si”, Phys. Rev. B, Vol. 23, May (1981)

[39] I. Santos, P. Castrillo, W. Windl, D. A. Drabold, L. Pelaz, and L. A. Marqués “Self-trapping in B-doped amorphous Si: Intrinsic origin of low acceptor efficiency”, Phy. Rev.B **81**, 033203, (2010); DOI: 10.1103/PhysRevB.81.033203

[40] R.A. Street “Doping and the Fermi Energy in Amorphous Silicon” Phy. Rev. Lett. 49, (1982)

[41] Fedders and Drabold; “Theory of boron doping in a-Si:H”, Phy. Rev. B 56, 1997-II

[42] D. Joung and S.I Khondakar “Efros-Shklovskii variable range hopping in reduced graphene oxide sheets of varying carbon sp2 fraction”, Phy. Rev. B **86**, (2012)

[43] Thejal Abraham, Chandrahas Bansal, J. Thampi Thanka Kumaran, and Ashok Chatterjee “Efros-Shklovskii variable range hopping transport in nano cluster metallic films”, J. Appl. Phys. 111, 104318, (2012)

[44] Shklovskii and Efros “Electronic Properties of Doped Semiconductor”, Springer

[45] L.J. van der Pauw, "A Method of Measuring Specific Resistivity and Hall Effect of Discs of Arbitrary Shapes," Philips Res. Repts. 13, 1-9 (1958).

[46] www.nist.gov/pml/semiconductor/hall.cfm

[47] Stefano Pitassi “Electrical and Optical Characterization of Non-crystalline silicon used an Infrared Detector at Room Temperature”, PhD Dissertation

[48] B. von Roedern, L. Ley, and M. Cardona “Photoelectron Spectra of Hydrogenated Amorphous Silicon”, Vol. 9, Num. 24, Phy. Rev.Lett. 12, Dec (1977)

[49] P.J. Zanzucchi, C.R. Wronski, and D.E. Carlson "Optical and photoconductive properties of discharge produced amorphous silicon", Journal of Applied Physics **48**, 5227 (2008);

[50] P.J. Zanzucci, C.R. Wronski, and D.E. Carlson, J. Appl. Phys. 47, (1977)

[51] B.Von Roedern, L. Ley, M. Cardona, "Photoelectron Spectra of Hydrogenated Amorphous Silicon", Phy. Rev. Lett. 39, (1977)

[52] K. Takahashi and M. Konagai: in Handbook of Amorphous Silicon Solar Cells, ed. E. F. R. D. Apps (Academic Press, London, 1986) p. 105

[53] A. M. Mazzone, "Boron impurities on a vicinal Si(100) surface: a study of structural properties and binding energies", Philosophical Magazine Letters, 82, (2002)

[54] A.G. Zabrodskii ," The Coulomb gap: The view of an Experimenter", Philosophical Magazine part B, 81:9,1131-1151]

[55] Anshuman Dalvi, N. Parvathala Reddy, S.C. Agarwal "The Meyer–Neldel rule and hopping conduction", Solid State Communications 152 (2012) 612–615, doi:10.1016/j.ssc.2012.01.018

[56] Zishan H. Khan "Electrical and optical properties of thin film of amorphous silicon nanoparticles", Applied Surface Science 255 (2009) 8874–8878

[57] Brodsky and Kaplan, "Hydrogen and the Density of States in amorphous silicon" J. of Non-Cryst. Solids, **32** (1979) 431-435

[58] H. Overhof "The Mott Memorial Lecture: Fundamental concepts in the physics of amorphous Semiconductors", J. of Non-Crystalline Solids **227–230** (1998) 15–22.

[59] Mark Fox, in "Optical Properties of Solids", PP 222

[60] Jeffrey S. Lannin, "Structural order and dynamics of amorphous Si and Ge", J. of Non-Cryst. Solids, **97 & 98** (1987) 203-206

[61] J. Forner and J.S. Lannin, "Short range order variations in amorphous silicon", J. of Non-Cryst. Solids, **106** (1988) 128-131.

[62] J. Forner and J.S. Lannin, "Radial distribution functions of amorphous silicon" Phys. Rev. B, **39** (1989) 5527-5532.

[63] R. Alben, E. Weair, J.E. Smith, Jr., and M.H. Brodsky, "Vibrational properties of amorphous Si and Ge", Phys. Rev. B **11** (1975) 2271.

[64] S. Gupta, R.S. Katiyar, S.Z. Weisz, I. Balberg, "The effect of light soaking on the structural order in a-Si:H" J. Non-Cryst. Solids, **266-269** (2000) 496-500.

[65] J.S. Lannin, L.J. Pilione, S.T. Kshirsagar, R. Messier and R.C. Ross, "Variable structural order in amorphous silicon", Phys. Rev.B **26** (1982) 3506-3509

[66] Maley, N. and Lannin, J. S., "Influence of hydrogen on vibrational and optical properties of a-$Si_{1-x}H_x$alloys", Phys. Rev.B **36** (1987) 1146-1152.

[67] C.R. Wronski and R.W. Collins, "Phase engineering of a-Si:H solar cells for optimized performance", Solar Energy, **77** (2004) 877–885.

[68] R. Saleh and N.H. Nickel, "Raman spectroscopy of B-doped microcrystalline silicon films", Thin Solid Films, **427** (2003) 266–269.

[69] H. Chen, M.H. Gullanara, W.Z. Shen, "Effects of high hydrogen dilution on the optical and electrical properties in B-doped nc-Si:H thin films", J. of Crystal Growth, **260** (2004) 91-101.

[70] Saravanapriyan Sriraman, Sumit Agarwal, Eray S. Aydil and Dimitrios Maroudas, "Mechanism of hydrogen-induced crystallization of amorphous silicon", Nature, **418** (2002) 62-65.

[71] N. Ross, K. Shrestha, O. Chyan, C.L. Littler, V.C. Lopes, and A.J. Syllaios (to be submitted for publication).

[72] Hishikawa, “Raman study on the variation of the silicon network of a-Si:H”, J. Appl. Phys., **62**, (1987) 3150-3155.

[73] P Danesh, B Pantchev, K Antonova, E Liarokapis, B Schmid, D Grambole and J Baran, “Hydrogen bonding and structural order in hydrogenated amorphous silicon prepared with hydrogen-diluted silane”, J. Phys. D: Appl. Phys. **37** (2004) 249–254.

[74] R. Tsu, J. Gonzalez-Hernandez, J.Doehler and S.R.Ovshinsky, “Order Parameters In a-Si Systems”, Solid State Communications, **46** (1983) 79-82.